Comput Geosci (2016) 20:975–996
DOI 10.1007/s10596-016-9572-5

ORIGINAL PAPER

A new methodology for computing ionic profiles and disjoining pressure in swelling porous media

Aline C. Rocha[1] · Marcio A. Murad[1] · Christian Moyne[2] · Saulo P. Oliveira[3] · Tien D. Le[1]

Received: 6 February 2015 / Accepted: 25 April 2016 / Published online: 20 May 2016

Abstract A new two-scale computational model is proposed to construct the constitutive law of the swelling pressure which appears in the modified form of the macroscopic effective stress principle for expansive clays saturated by an aqueous electrolyte solution containing multivalent ionic species. The microscopic non-local nanoscale model is constructed based on a coupled Poisson-Fredholm integral equation arising from the thermodynamics of inhomogeneous fluids in nanopores (Density Functional Theory), which governs the local electric double layer potential profile coupled with the ion-particle correlation function in an electrolytic solution of finite size ions. The local problem is discretized by invoking the eigenvalue expansion of the convolution kernel in conjunction with the Galerkin method for the Gauss-Poisson equation. The discretization of the Fredholm equation is accomplished by a collocation scheme employing eigenfunction basis. Numerical simulations of the local ionic profiles in rectangular cell geometries are obtained showing considerable discrepancies with those computed with Poisson-Boltzmann based models for point charges, particularly for divalent ions in calcium montmorillonite. The constitutive law for the disjoining pressure is reconstructed numerically by invoking the contact theorem within a post-processing approach. The resultant computational model is capable of capturing ranges of particle attraction characterized by negative values of the disjoining pressure overlooked by the classical electric double layer theory. Such results provide further insight in the role the swelling pressure plays in the modified macroscopic effective stress principle for expansive porous media.

Keywords Swelling clays · Effective stress principle · Disjoining pressure · Electric double layer · Integral equations · Statistical mechanics · Eigenvalue expansion · Basis eigenfunctions · Collocation schemes

✉ Marcio A. Murad
murad@lncc.br

[1] Laboratório Nacional de Computação Científica, Av. Getúlio Vargas, 333, Quitandinha, Petrópolis, CEP: 25651-075, Brazil

[2] LEMTA, Université de Lorraine, CNRS, 2, avenue de la Forêt de Haye, TSA 60604, F-54518, Vandoeuvre lès Nancy Cedex, France

[3] Departamento de Matemática, Universidade Federal do Paraná Curitiba, PR, CEP: 81531-980, Brazil

1 Introduction

Swelling ionized porous media are ubiquitous in nature and modern technologies and exhibit tremendous potential for applications in a wide range of fields including geo-environmental and materials sciences, geotechnical engineering, colloid chemistry, medical and life sciences. Historically, research on the computational modeling of such complex systems has focused on describing electro-chemo-mechanical couplings at a particular length scale of interest (ex. nanoscale in colloid science or macroscale in geotechnical engineering). Only recently, bridging between couplings at different scales in media composed of multiple levels of porosity has been accomplished [25, 30].

Understanding and modeling accurately the coupling between the chemistry of aqueous electrolyte solutions and mechanics in electrically charged porous media hinges on various relevant issues which demand strong multi-disciplinary efforts. Applications involve many still open problems in geosciences such as quality of groundwater

polluted by ionic contaminants coupled with mechanical stability of swelling active soils. More specifically in geo-environmental applications, containment of pollutants is an integral part of the protection strategy against contamination where expansive clays have been widely used in engineered barriers [38, 39]. Compacted bentonite consists of a geological material primarily composed of montmorillonite clay and has been used as a buffer in the design of repositories for isolation of high-level radioactive waste due to its ability to swell upon hydration and shrink upon desiccation, consequently preventing the barrier from the appearance of cracks with high permeability for contaminant migration which may degrade its performance. On the other hand, swelling soils cause major stability problems for rail and highway tunnels causing surface uplift and the heave of the tunnel floor. They may also cause severe damages to shallow foundations and overlying structures particularly low-rise buildings and buried pipelines [31]. Severe borehole-stability problems were caused by drilling in swelling shales in water-based drilling muds [34]. The chemo-mechanical couplings induced by the drilling fluid affect rock mechanical properties and stress around the wellbore. In particular, water migration in shale due to chemo-osmotic and electro-osmotic effects appears in a wide variety of wellbore stability models [24].

The swelling and contractive behavior of natural porous media such as clays and shales under chemical, electrical, and mechanical stimulations reflects the ability of these materials to transform electrical and chemical energy into mechanical work. Their effective response to perturbations in the geochemical environment, such as changes in temperature, pH, fluid composition, electrical, and mechanical loadings, need to be accurately modeled [35]. A characteristic feature of these materials is their sensitivity to the solutes present in the pore water, more precisely the nature of the cations in their exchange sites and the magnitude of the fixed surface charge which exert profound influence upon the mechanical properties. Thus, it is of primary importance to assess how hydraulic properties and volume changes respond to chemical perturbations in the pore fluid for a wide range of saline concentrations and solute types.

Despite the utmost importance of constructing realistic computational models for swelling clays, few works have rigorously addressed the interaction between electrochemistry and deformation at multiple scales [18]. Historically, the description of swelling phenomena has pursued purely macroscopic approaches by adding a chemical expansive component to the stress partitioning mechanisms ruled by the effective stress principle [6, 14]. Such chemical expansion stress aims at capturing macroscopically the mechanical effects of the electrolyte solution in nanopores delimited by macromolecules carrying fixed charges, whose behavior is described by the classical electrical double layer (EDL) theory [23, 44]. In order to capture in a precise manner the response of the expansive clay in the presence of mono and multivalent ionic species, the development of a proper nanoscale model of electrolyte solutions in the vicinity of electrically charged surfaces becomes essential along with the construction of the proper up-scaling technique to obtain the macroscopic response (see [15, 16]).

At the nanoscale, the negative fixed charges, located on the faces of the clay units, arise from the isomorphous substitutions of cations in the crystal lattice by solutes of lower valence. In order to fulfill electroneutrality, the concentration of counter-ions in the electrolyte solution varies rapidly in the nanopores achieving highest values in the vicinity of the charged surfaces. The classical electrical double layer theory describes the concentration of electrolytes near flat hard charged surfaces carrying a constant surface charge [17]. The well-established model developed by Gouy and Chapman [44] treats the ions as point charges with concentration obeying Boltzmann statistics and the electric potential satisfying the Poisson-Boltzmann problem (PB) [23]. Particularly, it has been shown that the Gouy-Chapman (GC) theory leads to much higher ionic concentrations near the wall as long-range Coulomb correlations predicted by the Boltzmann statistics can approach infinity with increasing electric potential [36]. In fact, real ions are not point-like charges and the PB-based framework, commonly embedded in the so-called mean-field theories, has shown severe limitations producing discrepancies in the ionic concentration profiles qualitatively unreliable compared to experiments [12, 13]. More precisely, the PB theory completely overlooks ionic correlations effects. In fact, ionic correlations in the diffuse double layer, entirely neglected in the GC approximation, are sometimes important and have motivated the development of more refined theories designed to incorporate short-range correlation effects. Since PB-based models neglect strong positional short-range finite size ion-ion correlations such theory always predicts electrostatic overestimated repulsion between likely charged particles [36]. A related phenomenon overlooked by the PB based theories is the counter-intuitive attraction between like-charged colloidal particles in the presence of higher valence ions which has been reported in numerous experimental observations [12, 13]. Theoretical approaches aiming at explaining the phenomenon of particle like-charge attraction proceed beyond the standard mean-field or PB-based theories by including the effects of fluctuations and correlations. The flaw of the PB formulation has naturally led to the development of more refined theories designed to incorporate short-range correlation effects. Among them, we give particular emphasis on models seated on Statistical Mechanics (SM) [10, 21] based on integral equation theories, more specifically on Ornstein-Zernike (OZ) supplemented by several closures such as Hypernetted Chain Approximation

(HNC), Percus-Yevick (PY), and Mean-Spherical approximation (MSA) [19, 20]. Other approaches such as Density Functional Theory (DFT) are based on Thermodynamics of Inhomogeneous Fluids where the free energy is described in terms of functional relations of ionic concentrations [9, 22, 41, 42]. Such non-local models incorporate the main features of the electric double layer and turned possible the computation of properties in an accurate fashion. In particular, the family of primitive models, where the solvent is treated as a dielectric continuum assigned with a dielectric constant and the ions treated as rigid spheres with charge located in their center, has successfully explained particle-like attractions for electrolyte solutions with higher valence ions [12, 13, 15, 19].

Given the solution of the electrochemistry problem at the nanoscale, the disjoining pressure introduced by Derjaguin and co-workers [5], whose magnitude governs the swelling of the medium, can be calculated within a post-processing approach by invoking the equilibrium of the fluid phase along with a constitutive relation for the stress tensor. Such computation can be accomplished within the framework of Irving and Kirkwood [3, 11, 15], who defined point-wise continuum stress fields from particle mechanics under the influence of pair potential interactions. The traction upon the solid matrix exerted by the stress tensor of the electrolyte solution can also be quantified by involving the contact theorem which states that the force in the vicinity of the wall is dominated by the osmotic kinetic (ideal gas) and electrostatic (Maxwell) components (see [15] for details).

The bridging between nanoscale models of electrolyte solutions containing multivalent ions, seated on SM-based integral equation theories, and the modified effective stress principle at the macroscale has only been accomplished recently by the authors, who adopted the homogenization technique of periodic structures to upscale a non-local integro-differential equation of Poisson-Fredholm type, build-up within the framework of the Density Functional Theory (DFT) (see [15, 16] for details). In a sequence of papers [25–30], the authors rigorously derived a modified macroscopic form of the effective stress principle showing, in addition to pore pressure and contact stress, the appearance of a swelling stress component which incorporates the electro-chemo mechanical couplings and rules the swelling/shrinking behavior of the medium. The computation of this quantity hinges on a non-local nanoscale problem which rules the local ionic profiles in the nanopores [15, 16]. Owing to the high complexity of this non-local nanoscale model, numerical solutions obtained so far remain restricted to the stratified microstructures of parallel particles of face to face contact, considering the 1D integral form of the Gauss-Poisson equation [15]. The generalization of the two-scale computational model for multidimensional local cell problems remains an open issue. The aim of this paper is to fill this gap. We propose herein a new improved numerical procedure for computing ionic profiles and the constitutive law for the disjoining pressure which adopts a suitable staggered algorithm between the Fredholm and Gauss-Poisson problem with Neumann boundary condition to avoid loss of uniqueness. The system of integral equations is discretized by a collocation scheme using basis functions constructed from the eigenfunctions associated with the convolution kernels. The nonlinear algebraic equation for the coefficients of the eigenvalue expansion is solved adopting a Picard-type scheme in conjunction with the Galerkin method coupled with Newton scheme for the nonlinear Gauss-Poisson problem. Numerical experiments illustrate the local ionic distribution for monovalent (sodium) and divalent (calcium) ions along with the eigenpairs associated with the convolution kernels. By invoking the contact theorem, we reconstruct numerically a generalized constitutive law for the swelling pressure, capable of capturing the regions of particle attraction for divalent ions. Numerical simulation illustrate the excellent accuracy of the computational procedure proposed herein.

2 Nanoscale model

In what follows, we present the necessary developments for constructing the nanoscale model governing the electro-chemo-mechanical coupling between an electrolyte solution containing finite size ions and electrically charged clay particles. We shall refer to as a particle a single solid phase composed of a flat sheet of montmorillonite clay, typical of the 2:1 arrangement, composed of one aluminum octahedral sheet sandwiched by two tetrahedral sheets of silicates.

2.1 Density functional theory

Consider the electrolyte solution occupying a nanopore domain subject to an exterior potential induced by both the presence of charges in the solid phase and the hard plane / hard spheres interaction $\phi_i(\boldsymbol{r})$ acting on ions of type i. Let the temperature T and the chemical potential μ_i of ion i be fixed. The procedure for computing the local density profile is based on minimization of a thermodynamic potential (grand canonical, free energy) of the inhomogeneous system which is given in terms of a functional relation of the local ionic density profile $\rho_i(\boldsymbol{r})$. By decomposing the free energy into its ideal $\mathcal{F}^{id}[\rho_i]$ and excess $\mathcal{F}^{ex}[\rho_i]$ components, the minimization method furnishes the local distribution (see [15] for details)

$$\rho_i(\boldsymbol{r})\Lambda_i^3 = \exp\left[\beta\left(\mu_i - \frac{\delta\mathcal{F}^{ex}[\rho_i]}{\delta\rho_i(\boldsymbol{r})} - \phi_i(\boldsymbol{r})\right)\right] \tag{1}$$

where Λ_i denotes the de Broglie wavelength of the ion i, $\beta = 1/k_B T$ with k_B the Boltzmann constant. The square brackets notation refers to functional dependence with δ the functional derivative [9]:

$$\delta\mathcal{F} = \mathcal{F}[\rho_i + \delta\rho_i] - \mathcal{F}[\rho_i] = \int \frac{\delta\mathcal{F}}{\delta\rho_i(\boldsymbol{r})}\delta\rho_i(\boldsymbol{r})d\boldsymbol{r}$$

which quantifies the change in $\mathcal{F}$ due to a perturbation in ρ_i at a particular point $\boldsymbol{r}$.

The complete characterization of $\rho_i(\boldsymbol{r})$ requires a representation for the excess intrinsic free energy component $\mathcal{F}^{ex}[\rho_i]$. Such quantity plays the role of a generating functional for a hierarchy of direct correlation functions $c^{(n)}(\boldsymbol{r}^n)$ [9]:

$$c_i^{(1)}(\boldsymbol{r}) = -\beta\frac{\delta\mathcal{F}^{ex}[\rho_i]}{\delta\rho_i(\boldsymbol{r})}\ , \tag{2}$$

$$c_{im}^{(2)}(\boldsymbol{r},\boldsymbol{r}') = c_{im}(\boldsymbol{r},\boldsymbol{r}') = \frac{\delta c^{(1)}(\boldsymbol{r})}{\delta\rho_m(\boldsymbol{r}')} = -\beta\frac{\delta^2\mathcal{F}^{ex}[\rho_i]}{\delta\rho_i(\boldsymbol{r})\delta\rho_m(\boldsymbol{r}')}\ . \tag{3}$$

Following [15], we proceed by representing the excess free energy relative to the reference bulk state. Thus denote the bulk state by the superscript b with excess free energy $(\mathcal{F}^b)^{ex}$, ion density ρ_i^b, and direct correlation function $c_{im}^2|^b = c_{im}^b$. By proceeding within the framework of a perturbation technique relative to the reference bulk state, adopting the well known Mean Spherical Approximation (MSA) [21], recalling that at local equilibrium with a bulk fluid $\mu_i = \mu_i^b$ and using the decomposition $(\mu_i^b)^{ex} = \mu_i^b - k_B T \ln\left[\Lambda_i^3\rho_i^b\right]$ [9], we obtain the integral representation for the local ion densities (see [15] for details)

$$\rho_i(\boldsymbol{r}) = \rho_i^b \exp\left[-\beta\phi_i(\boldsymbol{r}) + \sum_m \int \Delta\rho_m(\boldsymbol{r}')c_{im}^b(|\boldsymbol{r}-\boldsymbol{r}'|)d\boldsymbol{r}'\right]\ . \tag{4}$$

Now, introduce the ion-particle correlation functions $g_{\alpha i} := \rho_i(\boldsymbol{r})/\rho_i^b$ and $h_{\alpha i} := g_{\alpha i} - 1$ where the index α is related to the solid phase [20]. We then have

$$\Delta\rho_i(\boldsymbol{r}) = \rho_i - \rho_i^b = \rho_i^b g_{\alpha i}(\boldsymbol{r}) - \rho_i^b = \rho_i^b h_{\alpha i}(\boldsymbol{r})\ ,$$

which when combined with Eq. 4 gives

$$g_{\alpha i}(\boldsymbol{r}) = \exp\left[-\frac{\phi_i(\boldsymbol{r})}{k_B T} + \sum_m \rho_m^b \int h_{\alpha m}(\boldsymbol{r}')c_{im}^b(|\boldsymbol{r}-\boldsymbol{r}'|)d\boldsymbol{r}'\right]\ . \tag{5}$$

The complete determination of the ion-particle correlation function requires a constitutive law for the exterior potential $\phi_i(\boldsymbol{r})$ induced by the solid particle. Such quantity is decomposed into a long-range electrostatic interaction $\phi_i^{el}(\boldsymbol{r})$ and a hard plane/hard sphere interaction component $\phi_i^{hs}(\boldsymbol{r})$, treated separately through the characterization of an exclusion region defined by ion / clay particle distances smaller than the ion radius $d/2$ [15]. We then have

$$\phi_i(\boldsymbol{r}) = \phi_i^{hs}(\boldsymbol{r}) + \phi_i^{el}(\boldsymbol{r}) = \phi_i^{hs}(\boldsymbol{r}) + z_i\, e\, \psi_s(\boldsymbol{r})\ , \tag{6}$$

where

$$\phi_i^{hs}(\boldsymbol{r}) = \begin{cases} \infty & \text{in the exclusion zone} \\ 0 & \text{elsewhere} \end{cases}$$

and $\psi_s(\boldsymbol{r})$ the electrical potential generated by the net surface charge of the solid phase, z_i the valence of the ion i and e the proton charge. The net electric charge density in the fluid $q(\boldsymbol{r}')$ at point $\boldsymbol{r}'$ is defined by

$$\begin{aligned} q(\boldsymbol{r}') &:= \sum_m \rho_m(\boldsymbol{r}')\, z_m\, e = \sum_m \rho_m^b\, z_m\, e\, g_{\alpha m}(\boldsymbol{r}') \\ &= \sum_m \rho_m^b\, z_m\, e\left(1 + h_{\alpha m}(\boldsymbol{r}')\right) \\ &= \sum_m \rho_m^b\, z_m\, e\, h_{\alpha m}(\boldsymbol{r}')\ , \end{aligned} \tag{7}$$

as the electroneutrality condition in the bulk fluid enforces $\sum_m \rho_m^b\, z_m\, e = 0$. Within the Mean Spherical Approximation framework, the direct correlation function is decomposed as the sum of a long-range Coulombic term and a short-range component $\widetilde{c}_{im}(r)$ associated with the finite size of the ions (see Appendix B for details). We then have

$$c_{im}^{\mathrm{MSA}}(r) = \begin{cases} \widetilde{c}_{im}(r) - \dfrac{\beta z_i\, z_m\, e^2}{4\pi\,\widetilde{\varepsilon}\,\widetilde{\varepsilon}_0\, r} & \text{for } r < d \\ \\ -\dfrac{\beta z_i\, z_m\, e^2}{4\pi\,\widetilde{\varepsilon}\,\widetilde{\varepsilon}_0\, r} & \text{for } r > d\ , \end{cases} \tag{8}$$

where $\widetilde{\varepsilon}_0$ is the permittivity of the free space and $\widetilde{\varepsilon}$ the relative dielectric constant of the solvent (assumed constant). The representation for the short-range component due to the finite size of the ions is given in Eq. B.5 (see also [45, 46]).

Using the above decomposition and Eq. 6 in Eq. 5, introducing the ion charge $q_i = z_i\, e$ and the total electrical double layer potential $\psi(\boldsymbol{r})$:

$$\begin{aligned} \psi(\boldsymbol{r}) &:= \psi_s(\boldsymbol{r}) + \int \sum_m \frac{\rho_m^b\, z_m\, e\, h_{\alpha m}(\boldsymbol{r}')}{4\pi\,\widetilde{\varepsilon}\,\widetilde{\varepsilon}_0\,|\boldsymbol{r}-\boldsymbol{r}'|}\mathrm{d}\boldsymbol{r}' = \psi_s(\boldsymbol{r}) \\ &\quad + \int \frac{q(\boldsymbol{r}')}{4\pi\,\widetilde{\varepsilon}\,\widetilde{\varepsilon}_0\,|\boldsymbol{r}-\boldsymbol{r}'|}\mathrm{d}\boldsymbol{r}'\ , \end{aligned}$$

where Eq. 7 for the net charge density has been used, we obtain the final integral equation for the ion/particle distribution function [15, 20]

$$g_{\alpha i}(\boldsymbol{r}) = \exp\left[-\beta\, q_i\, \psi(\boldsymbol{r}) + \sum_m \rho_m^b \int h_{\alpha m}(\boldsymbol{r}')\,\widetilde{c}_{im}(|\boldsymbol{r}-\boldsymbol{r}'|)\,\mathrm{d}\boldsymbol{r}'\right]. \tag{9}$$

The above result consists of the classical Boltzmann distribution, given by the exponential dependence on ψ, supplemented by non-local ion size effects associated with the short-range correlation $\widetilde{c}_{im}(r)$.

2.2 Gauss-poisson equation

In order to compute $g_{\alpha i}(\boldsymbol{r})$ from Eq. 9, we need to solve the coupled electrochemical problem posed in terms of the electric potential and ion-particle correlation function. Denoting Ω_f, the nanopore domain occupied by the aqueous electrolyte solution, $\boldsymbol{E}$ the electric field of the EDL and recalling the net charge density in the fluid $q := \sum_m q_m \rho_m(\boldsymbol{r}) = \sum_m q_m \rho_m^b g_{\alpha m}(\boldsymbol{r})$, the classical Gauss-Poisson equation for the pair $\{\psi, \boldsymbol{E}\}$ reads

$$\begin{cases} \widetilde{\varepsilon}\widetilde{\varepsilon}_0 \nabla \cdot \boldsymbol{E} = \sum_i q_i \rho_i^b g_{\alpha i}(\boldsymbol{r}) \\ \boldsymbol{E} = -\nabla \psi \qquad \text{in } \Omega_f \,, \end{cases} \tag{10}$$

with the ion-particle correlation function given by the generalized Boltzmann distributions (9). Note that the classical EDL theory can be recovered from Eq. 9 by setting $\widetilde{c}_{im} = 0$ under the assumptions of point charge ions and symmetric electrolytes $z_+ = -z_- = z$. In this setting using electroneutrality in the bulk fluid $\sum_m \rho_m^b z_m = 0$, which yields $\rho_+^b = \rho_-^b = \rho^b$ and the classical Poisson-Boltzmann problem is recovered:

$$\widetilde{\varepsilon}\widetilde{\varepsilon}_0 \triangle \psi = 2\,\rho^b\, z\, e\, \sinh\left(\frac{z\, e\, \psi}{k_B T}\right) .$$

2.3 Summary of the nanoscale model

Our nanoscale model consists in: given the set of constants $\{\widetilde{\varepsilon}_0, \widetilde{\varepsilon}, \beta, q_i = z_i\, e\}$, the ion concentrations in the outer bulk solution $\{\rho_m^b\}$ satisfying the electroneutrality condition $(\sum_m q_m \rho_m^b = 0)$, and short-range ion-ion direct correlation functions $\widetilde{c}_{im}$ given by the MSA closure (8), find the microscopic fields $\{g_{\alpha i}, \psi\}$ satisfying

$$\begin{cases} \widetilde{\varepsilon}\widetilde{\varepsilon}_0\, \boldsymbol{\Delta}\psi = -\sum_i \rho_i^b\, q_i\, g_{\alpha i} \\ g_{\alpha i}(\boldsymbol{r}) = h_{\alpha i}(\boldsymbol{r}) + 1 = \exp\left\{ -\beta q_i \psi(\boldsymbol{r}) + \sum_m \rho_m^b \int \widetilde{c}_{im}\left(|\boldsymbol{r} - \boldsymbol{r}'|\right) h_{\alpha m}(\boldsymbol{r}') d\boldsymbol{r}' \right\} \end{cases} \tag{11}$$

along with the interface condition

$$\boldsymbol{E} \cdot \mathbf{n} = -\frac{\sigma}{\widetilde{\varepsilon}\widetilde{\varepsilon}_0} \quad \text{on} \quad \Gamma_{fs} \tag{12}$$

where Γ_{fs} denotes the boundary between fluid and solid, $\mathbf{n}$ the unit normal outward to Ω_f, and σ the constant surface charge of the clay particles which is related to q through the global electroneutrality condition

$$\int_{\Omega_f} q \, \mathrm{d}V = \sum_i \rho_i^b q_i \int_{\Omega_f} g_{\alpha i} \, \mathrm{d}V = -\int_{\Gamma_{fs}} \sigma \, \mathrm{d}S \,. \tag{13}$$

2.4 Mechanical equilibrium and disjoining pressure

We now present the post-processing approach for computing the disjoining pressure. Thus, denoting p_b the constant pressure of the outer bulk fluid at thermodynamic equilibrium with the electrolyte solution, the fluid stress tensor $\boldsymbol{\sigma}_f$ admits the decomposition [15]

$$\boldsymbol{\sigma}_f = -p_b\, \boldsymbol{I} - \boldsymbol{\Pi}_d \,,$$

where $\boldsymbol{I}$ is the unit tensor and $\boldsymbol{\Pi}_d$ the disjoining stress tensor which quantifies the excess in fluid stress relative to p_b. Following [15], the computation of the disjoining pressure can be accomplished using the contact theorem which states that within the exclusion zone the stress in the fluid phase admits the decomposition

$$\boldsymbol{\sigma}_f = \boldsymbol{\tau}_M + \boldsymbol{\sigma}_V \tag{14}$$

where $\boldsymbol{\tau}_M$ is the Maxwell tensor

$$\boldsymbol{\tau}_M = \frac{\widetilde{\varepsilon}\widetilde{\varepsilon}_0}{2}\left(2\boldsymbol{E} \otimes \boldsymbol{E} - E^2 \boldsymbol{I}\right) \tag{15}$$

with normal $(\boldsymbol{\tau}_M)_{nn} := \boldsymbol{\tau}_M \mathbf{n} \cdot \mathbf{n} = \sigma^2/(2\widetilde{\varepsilon}\widetilde{\varepsilon}_0)$, given by boundary condition (12), and $\boldsymbol{\sigma}_V$ a hard wall/sphere stress interaction term solely responsible for transmitting the osmotic kinetic component of the disjoining pressure (due to the collisions between the fluid molecules and the solid phase) through the exclusion zone. The equality between the normal $(\boldsymbol{\sigma}_V)_{nn}$ and kinetic components at the interface between the fluid domain Ω_f and the exclusion zone Γ_{fs}^* is stated in the contact theorem [3],[15] which gives

$$\boldsymbol{\sigma}_V = -k_B T \sum_i \rho_i \Big|_{\Gamma_{fs}^*} \mathbf{n} \otimes \mathbf{n} \,. \tag{16}$$

Using the above results in Eq. 14, the normal component of the fluid stress tensor at the wall is given by

$$\left(\boldsymbol{\sigma}_f\right)_{nn} = -k_B T \sum_i \rho_i \Big|_{\Gamma_{fs}^*} + \frac{\sigma^2}{2\widetilde{\varepsilon}\widetilde{\varepsilon}_0} \,, \tag{17}$$

In order to determine the disjoining pressure at the wall, we subtract the bulk pressure which is nothing but the pressure at the interface with the exclusion zone in the asymptotic

limit of a single particle with the same charge density σ, computed for large particle distances. This yields

$$(\boldsymbol{\Pi}_d)_{nn} = k_B\, T \sum_m \rho_m^b\, g_{\alpha m} - k_B\, T \sum_m \rho_m^b\, g_{\alpha m}\Big|_\infty \text{ on } \Gamma_{fs}^* \,, \tag{18}$$

where the symbol $\big|_\infty$ designates the computation of the quantity at infinity particle distances reflecting the behavior of the bulk fluid. The above result furnishes a general expression for the component of the disjoining pressure normal to the solid particles (see [15] for details).

It is worth noting that in the one-dimensional case of parallel particles, the equilibrium condition in the electrolyte solution implies that $(\boldsymbol{\Pi}_d)_{nn}$ is constant also in the exclusion zone (see [15] for details).

2.5 Macroscopic effective stress principle

Following [15], by upscaling the aforementioned microscopic model to the macroscale within the framework of the formal homogenization procedure leads to the two-scale form of the effective stress principle for expansive clays. At the homogenized scale, the clay particles and electrolyte solution are regarded as a solid/fluid mixture with co-existing phases and properties defined everywhere in the macroscopic domain Ω_M. In the absence of gravitational forces, the overall macroscopic equilibrium reads

$$\boldsymbol{\nabla}_x \cdot \boldsymbol{\sigma}_T^0 = 0 \;\text{ in } \Omega_M \,,$$

where $\boldsymbol{\sigma}_T^0$ is the macroscopic overall stress tensor of the mixture and the subscript x denotes the differential operator with respect to the macroscopic coordinate. The modified effective stress principle states the decomposition [29]

$$\boldsymbol{\sigma}_T^0 = -\boldsymbol{\alpha}\, p_b \boldsymbol{I} + \boldsymbol{C}_s\, \boldsymbol{\mathcal{E}}_{\boldsymbol{x}}\left(\mathbf{u}^0\right) - \boldsymbol{\Pi}^0 \,. \tag{19}$$

The first two components are well-known [2] with $\boldsymbol{\alpha}$ the Biot-Willis parameter, $\boldsymbol{C}_s$ the macroscopic fourth rank elastic tensor of the solid matrix, and $\boldsymbol{\mathcal{E}}_{\boldsymbol{x}}\left(\mathbf{u}^0\right)$ the strain of the porous matrix, given by symmetric part of the macroscopic displacement $\mathbf{u}^0$. The last term in the rhs is the electro-chemo-mechanical component which admits the local representation in the unit cell $Y = Y_s \cup Y_f$ with Y_s, Y_f the subdomains occupied by the nanopores and clay particles. We then have the local decompositions [27, 29]

$$\begin{cases} \boldsymbol{\Pi}^0 = \langle \boldsymbol{\Pi}_d \rangle + \phi_s\, \boldsymbol{\Pi}_S \\ \boldsymbol{\Pi}_S = -\langle \boldsymbol{\sigma}_\pi \rangle^s = -\left\langle \boldsymbol{c}_s\, \boldsymbol{\mathcal{E}}_y\left(\mathbf{u}_\pi^1\right)\right\rangle^s \end{cases} , \tag{20}$$

where $\phi_s = |Y_s| \,/\, |Y|$ is the volume fractions of the solid phase, $\boldsymbol{c}_s$ the elastic modulus of the clay particles, and $\langle\cdot\rangle$, $\langle\cdot\rangle^s = \phi_s^{-1}\langle\cdot\rangle$ the average and intrinsic average operators over the unit cell Y, respectively. The component $\boldsymbol{\Pi}_S$ designates the effective swelling stress which directly incorporates the traction boundary condition on the clay matrix induced by the disjoining pressure. Such quantity is computed by solving the local elasticity problem

$$\begin{cases} \boldsymbol{\nabla}_y \cdot \boldsymbol{\sigma}_\pi = 0 \\ \boldsymbol{\sigma}_\pi = \boldsymbol{c}_s\, \boldsymbol{\mathcal{E}}_y\left(\mathbf{u}_\pi^1\right) \text{ in } Y_s \end{cases} \tag{21}$$

along with the local traction condition

$$\boldsymbol{\sigma}_\pi\, \mathbf{n} = -\boldsymbol{\Pi}_d\, \mathbf{n} \text{ on } \partial Y_{fs} \,, \tag{22}$$

with ∂Y_{fs} the solid-fluid interface within the unit cell along with periodicity conditions. Thus, by solving the integro-differential problem at the nanoscale level along with post processing the disjoining stress and averaging to the macroscale, we obtained a new systematic framework for quantifying the effects of the swelling stress in the modified effective stress principle.

3 A new numerical scheme for discretizing the non-local nanoscale problem

We shall henceforth proceed by developing a new computational scheme for solving the non-local integro-differential nanoscale model to compute local distributions $(\rho_i, g_{\alpha i}, \psi)$ along with constructing the constitutive response of the swelling stress.

3.1 Staggered algorithm

We begin by proposing a consistent linearization procedure to discretize the nonlinear coupled integro-differential Eq. 11. Hereafter, we consider an electrolyte solution containing two types of ions (e.g., NaCl) of symmetric valences $z_+ = -z_- = z$ with reduced set of unknowns $\{\psi, g_{\alpha+}, g_{\alpha-}\}$ $(i = +, -)$ so that the electroneutrality constraint in the bulk fluid $(\sum_m \rho_m^b\, z_m = 0)$ implies $\rho_+^b = \rho_-^b = \rho^b$. In terms of the dimensionless electric potential $\psi_* = \beta\, e\, \psi$, the Gauss-Poisson problem reads

$$\begin{cases} \boldsymbol{\Delta}\psi_* = -\dfrac{\beta\, z\, e^2\, \rho^b}{\widetilde{\varepsilon}\,\widetilde{\varepsilon}_0}(g_{\alpha+} - g_{\alpha-}) & \text{in } Y_f \\ \boldsymbol{\nabla}\, \psi_* \cdot \mathbf{n} = -\dfrac{\beta\, e\, \sigma}{\widetilde{\varepsilon}\,\widetilde{\varepsilon}_0} & \text{on } \partial Y_{fs} \,, \end{cases} \tag{23}$$

with

$$g_{\alpha i}(\boldsymbol{r}) = \exp\left[-z_i\, \psi_*(\boldsymbol{r}) + \sum_m \rho_m^b \int \widetilde{c}_{im}(|\boldsymbol{r} - \boldsymbol{r}'|) h_{\alpha m}(\boldsymbol{r}')\, d\boldsymbol{r}'\right], \quad i = \{+, -\} \,. \tag{24}$$

A first attempt at solving the system in a staggered fashion would be in a Picard-type algorithm by computing the source term in the Poisson problem at previous iteration. However, such procedure leads to a Neumann problem for

ψ_* with loss of uniqueness. To avoid this shortcoming, we pursue an alternative strategy based on the decompositions

$$\begin{aligned} g_{\alpha+}(\boldsymbol{r}) &= \exp\left[-z\,\psi_*\right]\,\widetilde{g}_+(\boldsymbol{r})\,, \\ g_{\alpha-}(\boldsymbol{r}) &= \exp\left[+z\,\psi_*\right]\,\widetilde{g}_-(\boldsymbol{r})\,, \end{aligned} \tag{25}$$

with

$$\widetilde{g}_i(\boldsymbol{r}) := \exp\left[\sum_m \rho_m^b \int \widetilde{c}_{im}(|\boldsymbol{r}-\boldsymbol{r}'|)h_{\alpha m}(\boldsymbol{r}')d\boldsymbol{r}'\right], \quad i = \{+,-\}\,.$$

The alternative staggered algorithm is based on calculating at the previous iteration only the component $\widetilde{g}_i$ involving the short-range direct correlation, whereas the computation of the nonlinear term $\exp[-z_i\,\psi_*]$ is performed simultaneously with the electric potential by solving a nonlinear Poisson Boltzmann-type problem. Denoting $k = 1, 2, ...$ the iteration index associated with the staggered algorithm, we have

$$\begin{cases} \boldsymbol{\Delta}\psi_*^{(k)} = -\dfrac{\beta\,z\,e^2\,\rho^b}{\widetilde{\varepsilon}\,\widetilde{\varepsilon}_0}\left[\exp\left(-z\,\psi_*^{(k)}\right)\widetilde{g}_+^{(k-1)} - \exp\left(z\,\psi_*^{(k)}\right)\widetilde{g}_-^{(k-1)}\right] & \text{in } Y_f, \quad (26a) \\ \boldsymbol{\nabla}\,\psi_*^{(k)}\cdot\mathbf{n} = \dfrac{\beta\,e\,\sigma}{\widetilde{\varepsilon}\,\widetilde{\varepsilon}_0} & \text{on } \partial Y_{fs}\,, \quad (26b) \\ \widetilde{g}_i^{(k)}(\boldsymbol{r}) = \exp\left\{\sum_m \rho_m^b \int \widetilde{c}_{im}(|\boldsymbol{r}-\boldsymbol{r}'|)h_{\alpha m}^{(k)}(\boldsymbol{r}')d\boldsymbol{r}'\right\}, & i = \{+,-\}\,. \quad (26c) \end{cases}$$

It should be noted that the ψ_*-dependent source in the rhs of Eq. 26a overcomes the problem of lack of uniqueness in the Neumann problem. After solving for $\psi_*^{(k)}$, we need to compute the solution of the nonlinear integral Fredholm equation of second kind for $\widetilde{g}_i^{(k)}$, $i = \{+,-\}$. The initial choice of the iterative procedure is given by the absence of finite ion size effects so that $\widetilde{c}_{im} = 0$, implying $\widetilde{g}_i^{(0)} \equiv 1$, $i = \{+,-\}$, consequently leading to the nonlinear Poisson-Boltzmann problem for the electric potential at the first iteration

$$\begin{cases} \boldsymbol{\Delta}\psi_*^{(1)} = \dfrac{2\,\beta\,z\,e^2\,\rho^b}{\widetilde{\varepsilon}\,\widetilde{\varepsilon}_0}\sinh\left(z\,\psi_*^{(1)}\right) & \text{in } Y_f\,, \quad (27a) \\ \boldsymbol{\nabla}\,\psi_*^{(1)}\cdot\mathbf{n} = \dfrac{\beta\,e\,\sigma}{\widetilde{\varepsilon}\,\widetilde{\varepsilon}_0} & \text{on } \partial Y_{fs}\,. \quad (27b) \end{cases}$$

For the discretization of Eq. 26a, we consider the variational formulation along with the linearization using the Newton's method. Denoting $s = 1, 2, ...$ the index associated with the iterations in a Newton-type scheme we then have

$$\exp\left(\pm z\psi_*^{(k,s+1)}\right) \approx \exp\left(\pm z\psi_*^{(k,s)}\right) \pm z\exp\left(\pm z\psi_*^{(k,s)}\right)\left(\psi_*^{(k,s+1)} - \psi_*^{(k,s)}\right).$$

The variational formulation of the linearized problem consists in: denoting $\mathcal{W} = L^2(Y_f)$ the space of square integrable functions defined on the unit cell Y_f, $(\cdot,\cdot)$ the classical inner product in $\mathcal{W}$ and $\mathcal{V} = H^1 = \{f;\, f \in \mathcal{W} \text{ and } \partial f/\partial x_i \in \mathcal{W}\}$, given $\psi_*^{(k,s)} \in \mathcal{V}$ at the s-th iteration, find $\psi_*^{(k,s+1)} \in \mathcal{V}$ such that

$$a(\psi_*^{(k,s+1)}, \eta) = f(\psi_*^{(k,s)}, \eta) \quad \forall \eta \in \mathcal{V}\,, \tag{28}$$

with the bilinear form $a(\psi_*, \eta)$ and the functional $f(\psi_*, \eta)$ given by

$$\begin{aligned} a(\psi_*, \eta) = {} & (\nabla\psi_*, \nabla\eta) + \frac{\beta\,z^2\,e^2\,\rho^b}{\widetilde{\varepsilon}\,\widetilde{\varepsilon}_0}\left(\exp\left(-z\,\psi_*^{(k,s)}\right)\psi_*\,\widetilde{g}_+^{(k-1)}, \eta\right) \\ & + \frac{\beta\,z^2\,e^2\,\rho^b}{\widetilde{\varepsilon}\,\widetilde{\varepsilon}_0}\left(\exp\left(z\,\psi_*^{(k,s)}\right)\psi_*\,\widetilde{g}_-^{(k-1)}, \eta\right), \end{aligned}$$

and

$$\begin{aligned} f(\psi_*, \eta) = {} & \frac{\beta\,z\,e^2\,\rho^b}{\widetilde{\varepsilon}\,\widetilde{\varepsilon}_0}\left((1+z\,\psi_*)\exp\left(-z\,\psi_*\right)\widetilde{g}_+^{(k-1)}, \eta\right) \\ & + \frac{\beta\,e}{\widetilde{\varepsilon}\,\widetilde{\varepsilon}_0}\int_{\partial Y_{fs}} \sigma\,\eta\,d\Gamma \\ & - \frac{\beta\,z\,e^2\,\rho^b}{\widetilde{\varepsilon}\,\widetilde{\varepsilon}_0}\left((1-z\,\psi_*)\exp\left(z\,\psi_*\right)\widetilde{g}_-^{(k-1)}, \eta\right). \end{aligned}$$

For a fixed kth iteration associated with the coupling with the integral problem, the Newton scheme consists of an internal loop parametrized by the index s.

3.2 Discretization of the Fredholm equation in ordered rectangular nanopores

We shall now consider the discretization of the Fredholm equations of second kind (24) for a particular bidimensional rectangular cell geometry adopting a cartesian (x, y) coordinate system (Fig. 1). The particles are separated from each other by distances $2H_y$ and $2H_x$ in the y and x directions, respectively. The exclusion zone of thickness $d/2$ is characterized by flat shapes in the vicinity of each particle.

3.3 Ion distributions

Considering the EDL potential $\psi_*^{(k)}$ satisfying the Gauss-Poisson problem in the 2D rectangular domain and the short-range ion-ion direct correlation function given by the MSA closure (8), the integral (24) can be precisely represented in rectangular coordinates (see Appendix A for details)

$$\begin{aligned} g_{\alpha i}^{(k)}(x,y) \;=\; \exp\Bigg\{ & -z_i\,\psi_*^{(k)}(x,y) + \int_0^{H_x-\frac{d}{2}}\!\!\int_0^{H_y-\frac{d}{2}} \\ & \times K_{+i}(x,y,x',y')\,h_{\alpha+}^{(k)}(x',y')\,dy'\,dx' \\ & + \int_0^{H_x-\frac{d}{2}}\int_0^{H_y-\frac{d}{2}} K_{-i}(x,y,x',y') \\ & \times h_{\alpha-}^{(k)}(x',y')dy'dx' + J(x,y)\Bigg\}\,,\; i=\{+,-\}\,. \end{aligned} \tag{29}$$

The developments for obtaining the representations of the kernels $K_{\pm i}$ (A.9) and the function $J(x, y)$ (A.4) are given in Appendix A.

Hereafter, we present the numerical procedure for solving each equation in Eq. (26). The Poisson equation is discretized by the Galerkin procedure, whereas the approximation of the Fredholm equation is performed using the Collocation Method with basis functions suitably selected as the eigenfunctions associated with the eigenvalue problem of the kernels. The resultant nonlinear coupled system of algebraic equations is solved by a Picard-type scheme.

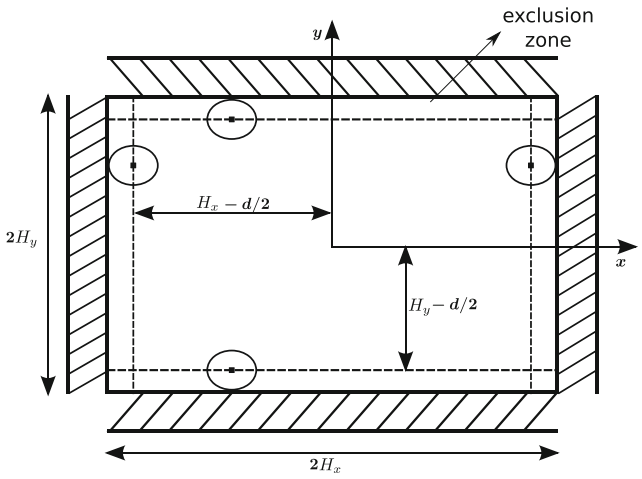

Fig. 1 Periodic cell with rectangular geometry

3.4 Galerkin method for the linearized gauss-poisson problem

At each Newton iteration, the weak form of Poisson problem for the electric potential (28) is discretized by the Galerkin method. Denote $\mathcal{V}_h$ the finite dimensional space of continuous piecewise polynomials of degree k_p associated with a partition of Y_f. The discrete form of the variational problem (28) reads: Given $\psi_{*h}^{(k,s)} \in \mathcal{V}_h$, find $\psi_{*h}^{(k,s+1)} \in \mathcal{V}_h$ such that:

$$a\left(\psi_{*h}^{(k,s+1)}, \eta_h\right) = f\left(\psi_{*h}^{(k,s)}, \eta_h\right) \quad \forall \eta_h \in \mathcal{V}_h\,. \tag{30}$$

In the notation that follows, we designate $\psi_{*h}^{(k)}$ the discrete solution obtained after convergence in the Newton iterations has been achieved for a given tolerance.

3.5 Discretization of the Fredholm integral equations

After computing $\psi_{*h}^{(k)}$, we proceed by discretizing the system of integral equations (29). By invoking the representation of the kernels in Appendix A, for symmetric ions $z_+ = z_- = z$ we have

$$\begin{aligned} K_{++}(x,y,x',y') &= K_{--}(x,y,x',y') = \overline{K}(x,y,x',y')\,, \\ K_{-+}(x,y,x',y') &= K_{+-}(x,y,x',y') = \widehat{K}(x,y,x',y')\,, \end{aligned} \tag{31}$$

with $\overline{K}(x, y, x', y')$ and $\widehat{K}(x, y, x', y')$ symmetric (see (A.9),(A.10)). Such symmetry property suggests the adoption of the eigenvalue expansion to obtain a robust discrete solution. The resultant eigenvalue problems are subsequently discretized by the Galerkin method combined with a Collocation eigenfunction scheme for the approximation of the Fredholm equations.

3.6 Discretization of the eigenvalue problems

Let us consider the following eigenvalue problem for the kernel $\overline{K}$:

$$\int_{Y_f} \overline{K}(x,y,x',y')\,\overline{u}^i(x',y')dy'\,dx' = \overline{\lambda}^i\,\overline{u}^i(x,y), \qquad (x,y) \in Y_f \quad i=1,\ldots, \tag{32}$$

From Eq. A.9, we have that the symmetric kernel $\overline{K}$ is square-integrable which implies that the operator defined in the lhs is compact in $L^2(Y_f)$ leading to the existence of

a countable set of real eigenvalues $\{\overline{\lambda}^i\}_{i=1}^{\infty}$ with associated linearly independent eigenfunctions $\{\overline{u}^i\}_{i=1}^{\infty}$ [8]. In a similar fashion to [32], we shall construct a basis of discrete eigenfunctions of the Galerkin approximation of Eq. 32.

Let $\mathcal{W}_h \subset \mathcal{W} = L^2(Y_f)$ be the space of continuous piecewise polynomial functions associated with the partition Y_h. Consider a cartesian mesh Y_h with number of nodes n same as eigenvalues with coordinates (x_p, y_p), $p = 1, \ldots, n$. The Galerkin method consists in: find $\left\{\overline{\lambda}_h^i, \overline{u}_h^i(x, y)\right\}_{i=1}^n \in \mathbb{R} \times \mathcal{W}_h$ such that, for any $\varphi_h \in \mathcal{W}_h$ and $1 \leq i \leq n$,

$$\int_{Y_f}\int_{Y_f} \overline{K}(x, y, x', y')\, \overline{u}_h^i(x', y')\varphi_h(x, y)dx'dy'\, dxdy = \overline{\lambda}_h^i \int_{Y_f} \overline{u}_h^i(x, y)\, \varphi_h(x, y)dydx\ .$$

The matrix formulation associated with the above discretization reads

$$\overline{A}\, \overline{\boldsymbol{u}}_h^i = \overline{\lambda}_h^i\, \overline{\boldsymbol{u}}_h^i\ , \quad i = 1, ..., n\ , \tag{33}$$

where the components of the matrix and vector are given by

$$\begin{aligned} \overline{A}_{pq} &= w_q \overline{K}(x_p, y_p, x_q, y_q), \\ \overline{\boldsymbol{u}}_{hp}^i &= \left[\overline{u}_h^i(x_p, y_p)\right], \quad p, q = 1, ..., n, \end{aligned}$$

with w_q the weights of the trapezoidal rule. Analogously, the discrete eigensystem for the kernel $\widehat{K}$ in matrix form reads as

$$\begin{aligned} \widehat{A}\, \widehat{\boldsymbol{u}}_h^i &= \widehat{\lambda}_h^i\, \widehat{\boldsymbol{u}}_h^i, \quad i = 1, ..., n\ , \\ \widehat{A}_{pq} &= w_q \widehat{K}(x_p, y_p, x_q, y_q), \\ \widehat{\boldsymbol{u}}_{hp}^i &= [\widehat{u}_h^i(x_p, y_p)], \quad p, q = 1, ..., n. \end{aligned} \tag{34}$$

The accuracy of the approximation (33)-(34) has been discussed in [33].

3.7 Collocation eigenfunction method for the Fredholm equation

Within the framework of the Collocation eigenfunction method, we consider the expansion of the discrete ion-particle correlation functions $\left(h_{\alpha+,h}^{(k)}, h_{\alpha-,h}^{(k)}\right)$ in terms of the eigenfunctions:

$$\begin{aligned} h_{\alpha+,h}^{(k)}(x, y) &= \sum_{i=1}^{n} \overline{a}_i^{(k)}\, \overline{u}_h^i(x, y)\ , \\ h_{\alpha-,h}^{(k)}(x, y) &= \sum_{i=1}^{n} \widehat{b}_i^{(k)}\, \widehat{u}_h^i(x, y)\ , \end{aligned} \tag{35}$$

with $\left\{\overline{a}_i^{(k)}, \widehat{b}_i^{(k)}\right\}_{i=1}^n$ the set of coefficients to be determined. It should be noted that the eigenfunctions are independent of the iteration k and therefore need to be computed only once, not requiring updating in the iterative process for solving (26).

Inserting the above expansion into the discrete form of the integral system (29) and adopting the quadrature rule gives

$$\begin{aligned} g_{\alpha+,h}^{(k)}(x, y) = \exp\Bigg\{ & - z\, \psi_{*h}^{(k)}(x, y) + \sum_{i=1}^{n} \overline{a}_i^{(k)} \sum_{q=1}^{n} w_q \\ & \times \overline{K}(x, y, x_q, y_q)\overline{u}_h^i(x_q, y_q) \\ & + \sum_{i=1}^{n} \widehat{b}_i^{(k)} \sum_{q=1}^{n} w_q\, \widehat{K}(x, y, x_q, y_q) \\ & \times \widehat{u}_h^i(x_q, y_q)\ + J(x, y)\Bigg\}\ , \end{aligned} \tag{36}$$

where $g_{\alpha+,h}^{(k)} = h_{\alpha+,h}^{(k)} + 1$. Within the context of the collocation method, the coefficients $\left\{\widehat{a}_i^{(k)}, \widehat{b}_i^{(k)}\right\}_{i=1}^n$ are determined by imposing the above equation at distinct collocation points (x_p, y_p), $p = 1, \ldots, n$:

$$\begin{aligned} g_{\alpha+,h}^{(k)}(x_p, y_p) = \exp\Bigg\{ & - z\, \psi_{*h}^{(k)}(x_p, y_p) + \sum_{i=1}^{n} \overline{a}_i^{(k)} \sum_{q=1}^{n} w_q \\ & \times \overline{K}(x_p, y_p, x_q, y_q)\overline{u}_h^i(x_q, y_q) \\ & + \sum_{i=1}^{n} \widehat{b}_i^{(k)} \sum_{q=1}^{n} w_q\, \widehat{K}(x_p, y_p, x_q, y_q) \\ & \times \widehat{u}_h^i\ (x_q, y_q) + J(x_p, y_p)\Bigg\}\ , 1 \leq p \leq n\ . \end{aligned}$$

Thus, using the discrete form of the eigenvalue problem given by Eq. 34 in the above result gives

$$\begin{aligned} g_{\alpha+,h}^{(k)}(x_p, y_p) = \exp\Bigg[& - z\, \psi_{*h}^{(k)}(x_p, y_p) + \sum_{i=1}^{n} \overline{a}_i^{(k)} \overline{\lambda}_h^i\, \overline{u}_h^i(x_p, y_p) \\ & + \sum_{i=1}^{n} \widehat{b}_i^{(k)} \widehat{\lambda}_h^i\, \widehat{u}_h^i(x_p, y_p) \\ & + J(x_p, y_p)\Bigg]\ , \ 1 \leq p \leq n\ . \end{aligned} \tag{37}$$

In an analogous manner, we adopt a similar expansion for $h_{\alpha-,h}^{(k)}$. In addition, introduce the crossed expansions

$$\begin{aligned} h_{\alpha+,h}^{(k)}(x, y) &= \sum_{i=1}^{n} \widehat{a}_i^{(k)}\, \widehat{u}_h^i(x, y)\ , \\ h_{\alpha-,h}^{(k)}(x, y) &= \sum_{i=1}^{n} \overline{b}_i^{(k)}\, \overline{u}_h^i(x, y)\ . \end{aligned} \tag{38}$$

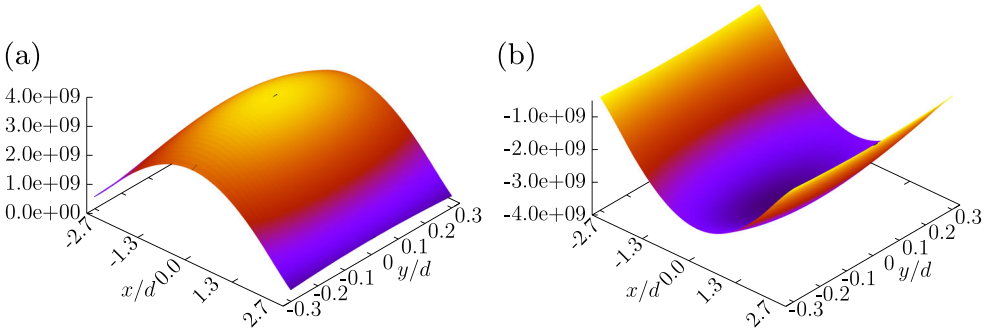

Fig. 2 Eigenfunctions associated with the kernels. **a** $\overline{K}$ and **b** $\widehat{K}$

By proceeding in a similar fashion to the derivation of (37) using the above expansions, we arrive at the following approximation of (29) with $i = +, -$

$$g^{(k)}_{\alpha-,h}(x_p, y_p) = \exp\left[z\,\psi^{(k)}_{*h}(x_p, y_p) + \sum_{i=1}^{n} \widehat{a}^{(k)}_i \widehat{\lambda}^i_h\, \widehat{u}^i_h(x_p, y_p) + \sum_{i=1}^{n} \overline{b}^{(k)}_i \overline{\lambda}^i_h\, \overline{u}^i(x_p, y_p) + J(x_p, y_p)\right],\ 1 \le p \le n\,. \tag{39}$$

Therefore, we introduced the two representations (35), (38) for $h^{(k)}_{\alpha+,h}$ and $h^{(k)}_{\alpha-,h}$ which leads to $4n$ unknown coefficients: $\{\overline{a}^{(k)}_i, \widehat{a}^{(k)}_i, \overline{b}^{(k)}_i, \widehat{b}^{(k)}_i\}_{i=1}^n$. For the closure, we adopt a suitable change of basis to obtain direct relations between $\left(\{\overline{a}^{(k)}_i\}_{i=1}^n, \{\overline{b}^{(k)}_i\}_{i=1}^n\right)$ and $\left(\{\widehat{a}^{(k)}_i\}_{i=1}^n, \{\widehat{b}^{(k)}_i\}_{i=1}^n\right)$. Denoting $[\boldsymbol{I}]^{\widehat{u}^i_h}_{\overline{u}^i_h} = [d_{ij}]$ the rotation matrix associated with the change of basis $[\widehat{u}^i_h] \rightarrow [\overline{u}^i_h]$ and making use of the notation

$$\left[h^{(k)}_{\alpha+,h}\right]_{\overline{u}^i_h} = \begin{bmatrix} \overline{a}^{(k)}_1 \\ \vdots \\ \overline{a}^{(k)}_n \end{bmatrix},\ \left[h^{(k)}_{\alpha+,h}\right]_{\widehat{u}^i_h} = \begin{bmatrix} \widehat{a}^{(k)}_1 \\ \vdots \\ \widehat{a}^{(k)}_n \end{bmatrix},\ \left[h^{(k)}_{\alpha-,h}\right]_{\overline{u}^i_h} = \begin{bmatrix} \overline{b}^{(k)}_1 \\ \vdots \\ \overline{b}^{(k)}_n \end{bmatrix},\ \left[h^{(k)}_{\alpha-,h}\right]_{\widehat{u}^i_h} = \begin{bmatrix} \widehat{b}^{(k)}_1 \\ \vdots \\ \widehat{b}^{(k)}_n \end{bmatrix},$$

for the coefficients of $h^{(k)}_{\alpha+,h}$ and $h^{(k)}_{\alpha-h}$ with respect to the bases $[\overline{u}^i_h]$ and $[\widehat{u}^i_h]$, respectively, we have

$$\left[h^{(k)}_{\alpha+,h}\right]_{\overline{u}^i_h} = [\boldsymbol{I}]^{\widehat{u}^i_h}_{\overline{u}^i_h} \left[h^{(k)}_{\alpha+,h}\right]_{\widehat{u}^i_h},$$
$$\left[h^{(k)}_{\alpha-,h}\right]_{\overline{u}^i_h} = [\boldsymbol{I}]^{\widehat{u}^i_h}_{\overline{u}^i_h} \left[h^{(k)}_{\alpha-,h}\right]_{\widehat{u}^i_h}.$$

Thus, we have the additional restrictions

$$\overline{a}^{(k)}_i = \sum_{j=1}^{n} d_{ij}\, \widehat{a}^{(k)}_j, \quad \overline{b}^{(k)}_i = \sum_{j=1}^{n} d_{ij}\, \widehat{b}^{(k)}_j\,. \tag{40}$$

By substituting (40) in Eqs. 37 and 39, we arrive at

$$g^{(k)}_{\alpha+,h}(x_p, y_p) = \exp\left[-z\psi^{(k)}_{*h}(x_p, y_p) + \sum_{i,j=1}^{n} d_{ij}\, \widehat{a}^{(k)}_j \overline{\lambda}^i_h\, \overline{u}^i_h(x_p, y_p) + \sum_{i=1}^{n} \widehat{b}^{(k)}_i \widehat{\lambda}^i_h\, \widehat{u}^i_h(x_p, y_p) + J(x_p, y_p)\right], \tag{41a}$$

$$g^{(k)}_{\alpha-,h}(x_p, y_p) = \exp\left[z\,\psi^{(k)}_{*h}(x_p, y_p) + \sum_{i=1}^{n} \widehat{a}^{(k)}_i \widehat{\lambda}^i_h\, \widehat{u}^i_h(x_p, y_p) + \sum_{i,j=1}^{n} d_{ij}\, \widehat{b}^{(k)}_j \overline{\lambda}^i_h\, \overline{u}^i_h(x_p, y_p) + J(x_p, y_p)\right], 1 \le p \le n\,. \tag{41b}$$

The last step consists in inserting the expansions (35)(b) and (38)(a) for $g^{(k)}_{\alpha+,h} = h^{(k)}_{\alpha+,h} + 1$ and $g^{(k)}_{\alpha-,h} = h^{(k)}_{\alpha-,h} + 1$, respectively, in the above lhs. This yields the following nonlinear system of $2n$ equations for the unknowns

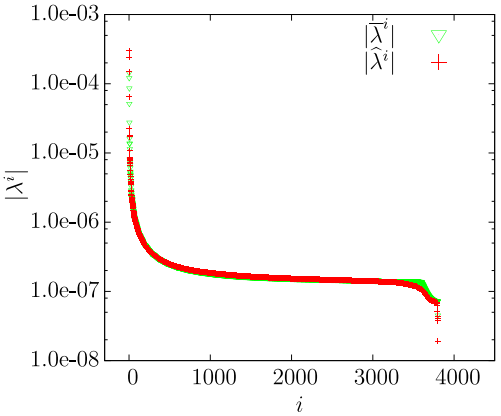

Fig. 3 Decay of the eigenvalues associated with the kernels $\overline{K}$ and $\widehat{K}$

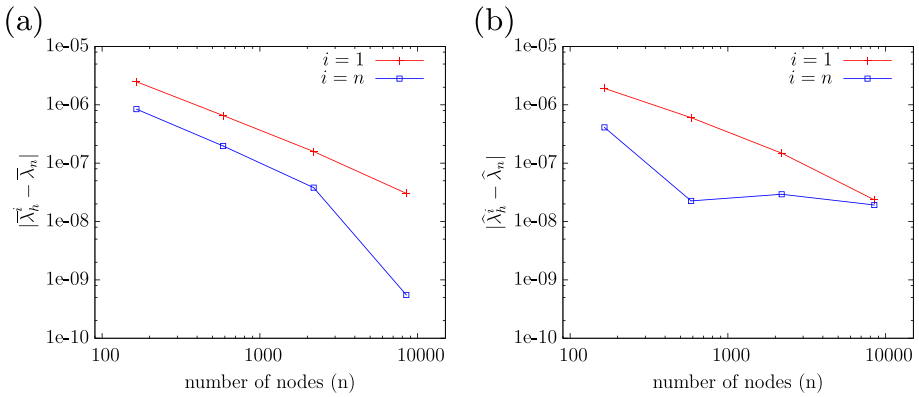

Fig. 4 Error of first and last eigenvalues associated with the kernels. **a** $\overline{K}$ and **b** $\widehat{K}$ computed with grids with $n = (8j+1) \times (j+1)$ nodes, $j = 4, 8, 16, 32$

$\{\widehat{a}_i^{(k)}, \widehat{b}_i^{(k)}\}_{i=1}^n$ at the kth iteration with the Gauss-Poisson problem:

$$\sum_{i=1}^n \widehat{a}_i^{(k)} \widehat{u}_h^i(x_p, y_p) = \exp\left[-z\, \psi_{*h}^{(k)}(x_p, y_p) + \sum_{i,j=1}^n d_{ij} \widehat{a}_j^{(k)} \overline{\lambda}_h^i \overline{u}_h^i(x_p, y_p) + \sum_{i=1}^n \widehat{b}_i^{(k)} \widehat{\lambda}_h^i \widehat{u}_h^i(x_p, y_p) + J(x_p, y_p) \right] - 1 , \quad (42a)$$

$$\sum_{i=1}^n \widehat{b}_i^{(k)} \widehat{u}_h^i(x_p, y_p) = \exp\left[z\, \psi_{*h}^{(k)}(x_p, y_p) + \sum_{i=1}^n \widehat{a}_i^{(k)} \widehat{\lambda}_h^i \widehat{u}_h^i(x_p, y_p) + \sum_{i,j=1}^n d_{ij} \widehat{b}_j^{(k)} \overline{\lambda}_h^i \overline{u}_h^i(x_p, y_p) + J(x_p, y_p) \right] - 1 , \; 1 \le p \le n . \quad (42b)$$

Once the coefficients $\{\widehat{a}_i^{(k)}, \widehat{b}_i^{(k)}\}_{i=1}^n$ have been computed, the discrete ion-particle correlation functions can be obtained in a straightforward fashion from the eigenpair expansion

$$g_{\alpha+,h}^{(k)}(x_p, y_p) = h_{\alpha+,h}^{(k)}(x_p, y_p) + 1 = \sum_{i=1}^n \widehat{a}_i^{(k)} \widehat{u}^i(x_p, y_p) + 1 , \quad (43a)$$

$$g_{\alpha-,h}^{(k)}(x_p, y_p) = h_{\alpha-,h}^{(k)}(x_p, y_p) + 1 = \sum_{i=1}^n \widehat{b}_i^{(k)} \widehat{u}^i(x_p, y_p) + 1, \; 1 \le p \le n . \quad (43b)$$

After computing the ion-particle correlation function within the iterative procedure (26) make use of decomposition (25) for $g_{\alpha i}^{(k)}(x, y)$ in the source term of the Gauss-Poisson problem and update only the components independent of the electric potential in Eq. 41

$$\widetilde{g}_+^{(k)}(x_p, y_p) = \exp\left[\sum_{i,j=1}^n d_{ij}\, \widehat{a}_j^{(k)} \overline{\lambda}_h^i\, \overline{u}_h^i(x_p, y_p) + \sum_{i=1}^n \widehat{b}_i^{(k)} \widehat{\lambda}_h^i\, \widehat{u}_h^i(x_p, y_p) + J(x_p, y_p) \right] , \quad (44a)$$

$$\widetilde{g}_-^{(k)}(x_p, y_p) = \exp\left[\sum_{i=1}^n \widehat{a}_i^{(k)} \widehat{\lambda}_h^i\, \widehat{u}_h^i(x_p, y_p) + \sum_{i,j=1}^n d_{ij}\, \widehat{b}_j^{(k)} \overline{\lambda}_h^i\, \overline{u}_h^i(x_p, y_p) + J(x_p, y_p) \right] , 1 \le p \le n . \quad (44b)$$

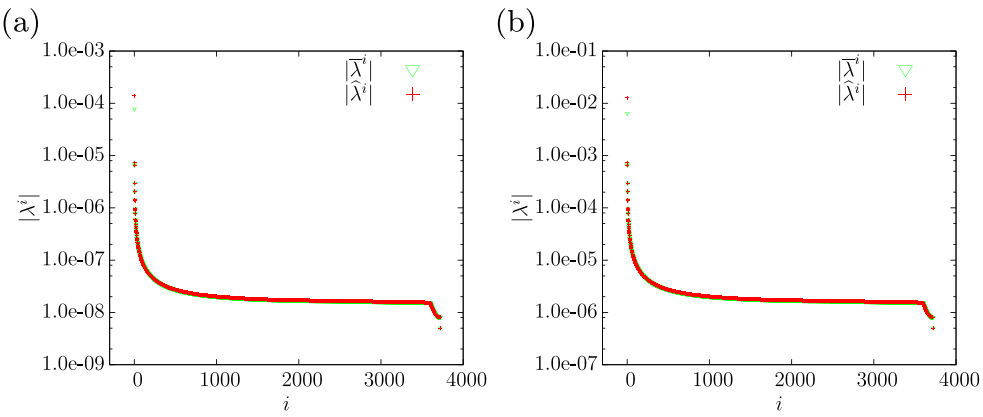

Fig. 5 Decay of the eigenvalues associated with the kernels $\overline{K}$ and $\widehat{K}$. **a** c_b =0.001 M and **b** c_b = 0.1 M

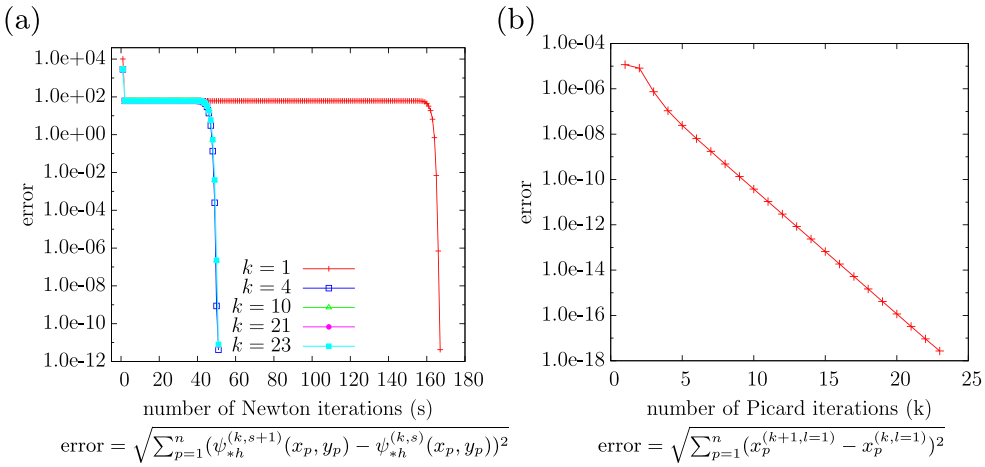

Fig. 6 Convergence of the iterative schemes with k for $l = 1$. **a** Newton (30) and **b** Picard (45)

3.8 Picard's method for the nonlinear system

Equations 42a and 42b give rise to a nonlinear system of algebraic equations for the coefficients which can be solved by the iterative Picard's scheme. Thus, introducing the iteration index l associated with the nonlinearity and $\mathbf{x}^{(k,l)} = [\widehat{a}_i^{(k,l)}, \widehat{b}_i^{(k,l)}]^T$, the vector of unknowns at the lth iteration along with the vector associated with the rhs of Eq. 42 $\boldsymbol{b}(\mathbf{x}^{(k,l)}) = [\boldsymbol{b}_+^{(k,l)}(\psi_{*h}^{(k,l)}, \mathbf{x}^{(k,l)}), \boldsymbol{b}_-^{(k,l)}(\psi_{*h}^{(k,l)}, \mathbf{x}^{(k,l)})]^T$ and the matrix

$$B := \begin{bmatrix} \overline{B} & 0 \\ 0 & \widehat{B} \end{bmatrix}, \quad \begin{cases} \overline{B}_{p,i} = \overline{u}_h^i(x_p, y_p) \\ \widehat{B}_{p,i} = \widehat{u}_h^i(x_p, y_p) \end{cases},$$

the linearized form of Eq. 42 posed at the collocation points reads as

$$B\,\mathbf{x}^{(k,l+1)} = \boldsymbol{b}(\psi_{*h}^{(k,l)}, \mathbf{x}^{(k,l)}), \quad l = 1, 2, \ldots . \tag{45}$$

The above system is solved in an internal loop for each frozen iteration k associated with the coupling with the Gauss-Poisson problem.

3.9 Summary of the staggered algorithm

For the sake of completeness, we present the final staggered algorithm for the resolution of the coupled Poisson-Fredholm integro-differential system:

1. Compute the eigenpairs $\left\{\overline{\lambda}_h^i, \overline{u}_h^i(x_p, y_p)\right\}_{p,i=1}^n$ and $\left\{\widehat{\lambda}_h^i, \widehat{u}_h^i(x_p, y_p)\right\}_{p,i=1}^n$ at the collocation points by solving (33)-(34);
2. At the first iteration, choose $\widetilde{g}_i^{(0)} \equiv 1$ and compute $\psi_{*h}^{(1)}$ by solving the Poisson-Boltzmann problem (27) in the iterative form (30) until convergence in s is achieved within the Newton method;
3. For $k = 1, 2, \ldots,$:
   - 3.1 Compute the coefficients $\mathbf{x}^{(k)} = \left\{\widehat{a}_i^{(k)}, \widehat{b}_i^{(k)}\right\}_{i=1}^n$ by solving the nonlinear algebraic system (42) in the iterative form (45) within the following procedure: For $l = 1, 2, \ldots,$:
     - (a) Given $\mathbf{x}^{(k,l)}$, solve the linear system (45) for $\mathbf{x}^{(k,l+1)}$;
     - (b) With $\mathbf{x}^{(k,l+1)}$, update the source terms $\left\{\widetilde{g}_i^{(k,l+1)},\ i = +, -\right\}$ using (44);
     - (c) Return to (a) till $||\mathbf{x}^{(k,l+1)} - \mathbf{x}^{(k,l)}|| < \text{tol}_{\mathbf{x}}$ for a given tolerance $\text{tol}_{\mathbf{x}}$.
   - 3.2 Update $\left\{g_{\alpha+,h}^{(k)},\ g_{\alpha-,h}^{(k)}\right\}$ using (41);
   - 3.3 Given $\widetilde{g}_i^{(k)}$, $i = \{+, -\}$, update the electric potential $\psi_{*h}^{(k+1)}$ in the nonlinear Poisson problem;
   - Return to 3.1 till $||\psi_{*h}^{(k+1)} - \psi_{*h}^{(k)}|| < \text{tol}_{\psi}$ is achieved for a given tolerance tol_{ψ}.

An important feature underlying the above scheme is that the inner Newton algorithm for the Gauss-Poisson problem needs to be performed for each update of the source term in the Picard scheme. We also remark that in the composed scheme, the iterations associated with the two Picard algorithms need to be performed sequentially to avoid divergence. Therefore, in the simulations that follow, the internal loop in l is performed restricted to $l = 1$.

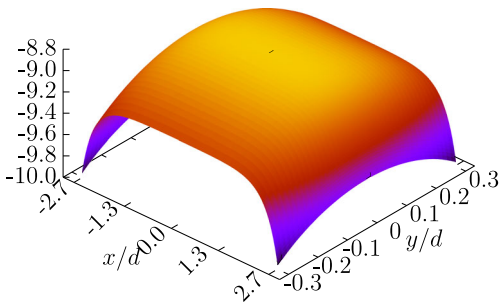

Fig. 7 Dimensionless electric potential profile

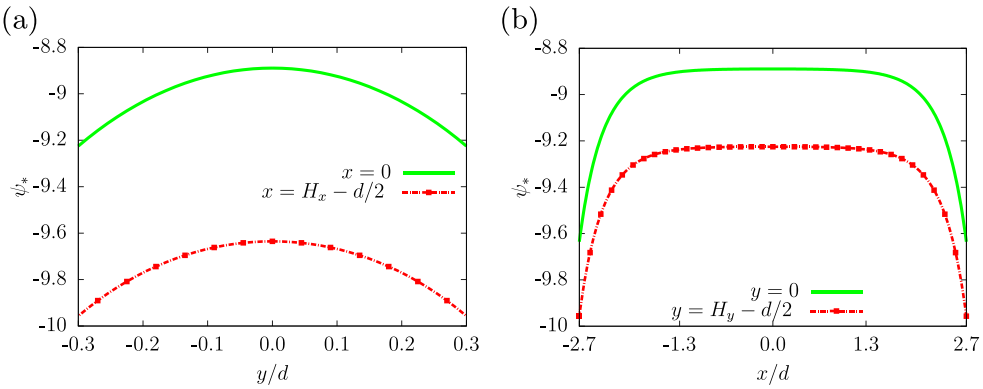

Fig. 8 Dimensionless electric potential distribution over the planes (**a**) $x = 0$ and $x = H_x - d/2$; (**b**) $y = 0$ and $y = H_y - d/2$

4 Numerical results

The aforementioned computational model gives rise to a new methodology for computing electro-chemomechanical couplings in swelling porous media saturated by aqueous electrolyte solutions with multivalent ions. In order to validate the new proposed approach, we shall henceforth present numerical simulations of the non-local nanoscale model for the particular ordered microstructures of the unit cell Y aiming at illustrating local ion distributions and the numerical constitutive law of the disjoining pressure.

In the discretization of the Poisson problem by the Galerkin method, we make use of bilinear elements, whereas for the solution of the integral equation for the coefficients, we adopt collocation points that coincide with the number of eigenfunctions adopted in the truncated expansions (38). In all simulations, we adopt a constant surface charge $\sigma = -0.1\,\mathrm{C\,m^{-2}}$.

4.1 Eigenpairs

We begin by depicting the spectrum of the eigenvalues along with the profile of some eigenfunctions. Note that the kernels are well conditioned in the sense that the eigenvalues are clustered away from zero. In spite of that, we cannot ensure positive definiteness and therefore, the eigenvalues are shown in absolute values.

In Figs. 2 and 3, we depict two eigenfunctions associated with kernels $\overline{K}$ and $\widehat{K}$ along with the decay of the absolute value of the eigenvalues $\{\overline{\lambda}_h^i\}_{i=1}^n$, $\{\widehat{\lambda}_h^i\}_{i=1}^n$ respectively, for monovalent ions and $c_b = 0.001\mathrm{M}$, $H_x/d = 3.2$, $H_y/d = 0.8$, adopting a mesh with 180×20 elements. For both $\overline{K}$ and $\widehat{K}$, the decay of the eigenvalues is abrupt at both ends of the spectrum. Conversely, away from the ends, we may observe slow decay with a non negligible ratio between the magnitude of the smallest and largest eigenvalue. Therefore, we keep track of the n eigenfunctions in the discrete basis.

In order to assess the accuracy of the computation of the eigenvalues, we compute the errors of the first and last eigenvalues with respect to the grid size. Figure 4 shows the dependence of these errors for the two kernels with four levels of mesh refinement. The exact eigenvalues are calculated with the finest mesh (512×64 elements). The decay of the error of the first eigenvalue has a clear trend in both kernels whereas for the last eigenvalue, owing to its smaller magnitude, the error exhibits much higher sensitivity to the discretization which may deteriorate trends in the decay.

Figure 5 compares the decay of the eigenvalues of the kernels $\overline{K}$ and $\widehat{K}$ for the two salinities $c_b = 0.001\mathrm{M}$ and $c_b = 0.1\mathrm{M}$ in the square domain ($H_x/d = H_y/d = 0.8$).

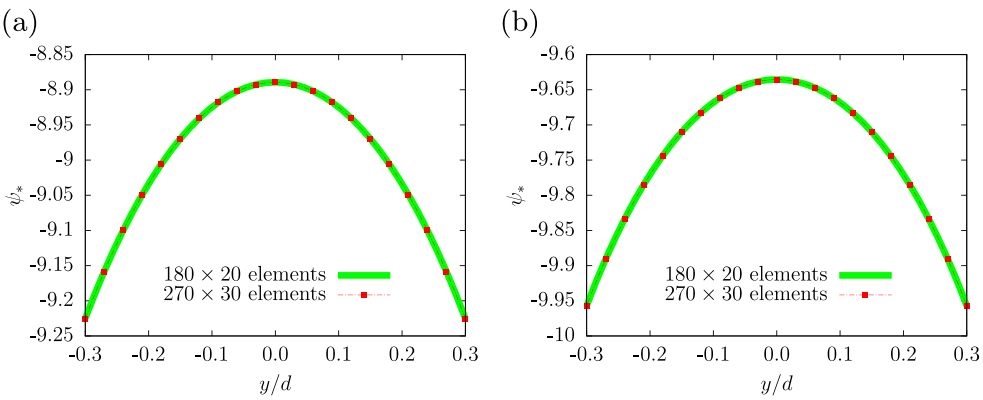

Fig. 9 Dimensionless electric potential distribution over the planes (**a**) $x = 0$ and (**b**) $x = H_x - d/2$ for two discretizations

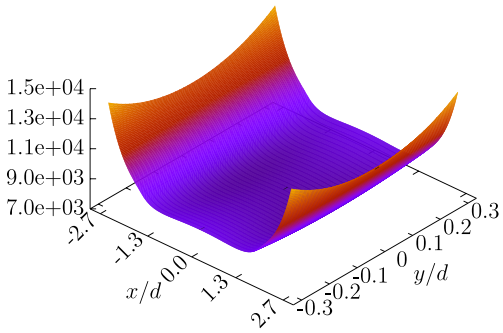

Fig. 10 Monovalent cationic profile computed with the DFT/MSA approach

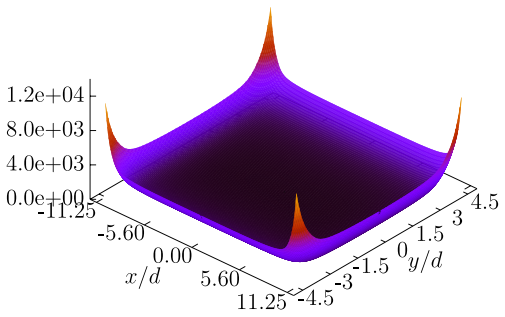

Fig. 12 Bi-dimensional cationic profile computed with DFT/MSA

From Eq. A.5, we may observe linear behavior on $c_b = \rho^b/N_a$ (where N_a is the Avogadro number) which is illustrated by the factor of 100 in the spectra shown in Figs. 5a and b.

4.2 Convergence of the staggered algorithm

The subsequent numerical results displayed in Fig. 6 aim at illustrating the performance of the iteration schemes for handling the nonlinearities. Convergence results are presented for the case of monovalent ions and $c_b = 0.001$M, $H_x/d = 3.2$, $H_y/d = 0.8$ adopting a mesh with 180×20 elements. In Fig. 6a, we depict the decay of the difference (in the euclidean norm) between the electric potential in two consecutive iterations of the Newton scheme parametrized by the number of k-iterations of the Picard scheme for the Gauss-Poisson problem. With the exception of the first iteration in k, fast convergence in the Newton scheme is observed. Moreover, the error decay for the coefficients in the expansion of the ion-particle correlation function in Eq. (43) with the number of k-iterations is depicted in Fig. 6b illustrating the convergence of the Picard scheme.

4.3 Ionic profiles

We now display the ion distributions considering the local rectangular arrangements of Fig. 1. The profiles are depicted in the reduced domain $[0, H_x - d/2] \times [0, H_y - d/2]$ not including the exclusion zone where ion concentration vanishes, adopting a mesh with 180×20 elements. Firstly, we consider the monovalent case $z_+ = -z_- = 1$ with the distance between the particles in the y-direction ($H_y/d = 0.8$) much smaller compared to that in the x-direction ($H_x/d = 3.2$). In Fig. 7, we depict the bidimensional profile of the dimensionless electric potential for $c_b = 0.001$ M. The potential attains minimum absolute value at the center of the rectangular domain $x = y = 0$ where the electric field vanishes. Sharp layers are observed in the vicinity of the charged surfaces where ψ_* reaches maximum negative values. The effects of the ion-ion correlations due to finite ion size are more pronounced for small particle distances where the correlations act to reduce the magnitude of the source term in the Gauss-Poisson problem decreasing the y-component of the electric field compared to the x-component and also the intensity of the boundary layer at $y = \pm(H_y - d/2)$ compared to $x = \pm(H_x - d/2)$ where the PB solution provides a good approximation. Such behavior is illustrated more precisely in Fig. 8 which shows the

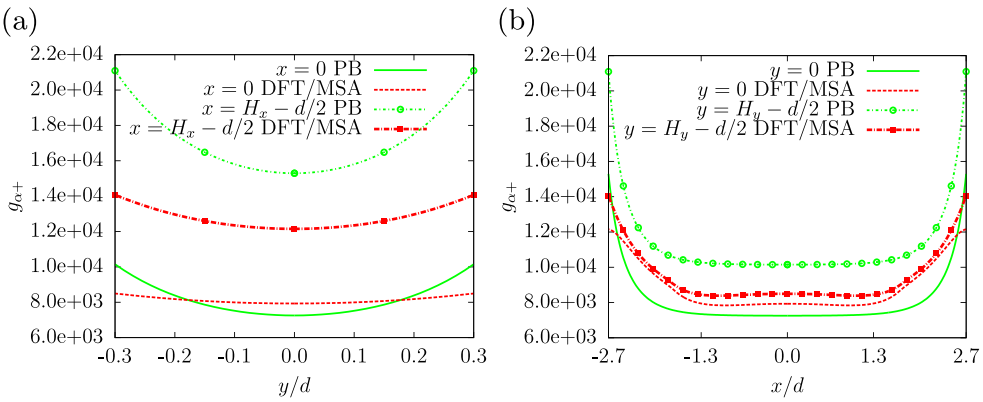

Fig. 11 Comparison between the one-dimensional ionic profiles obtained with PB and DFT/MSA approaches

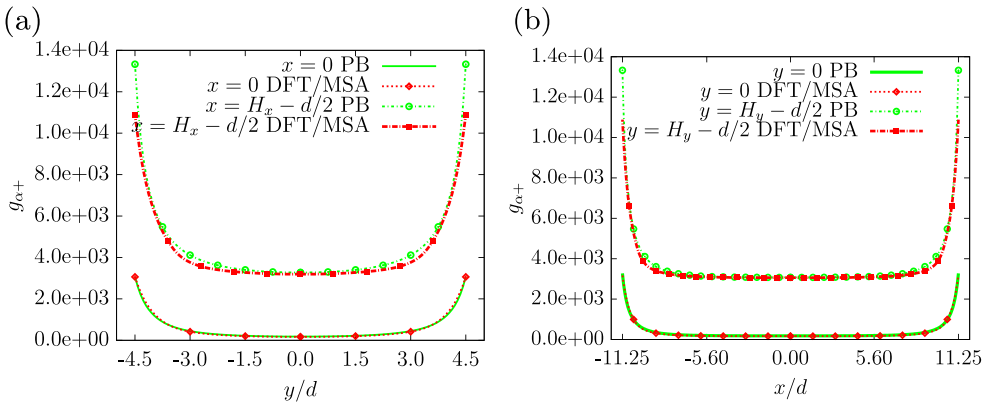

Fig. 13 Comparison between the one-dimensional ionic profiles computed with PB and DFT/MSA procedures

1D profiles along the coordinate planes (x and y constant), respectively. The influence of mesh refinement in the accuracy of the dimensionless electric potential profile is shown in Fig. 9. We may observe good agreement between the results obtained with two levels of refinement showing the accuracy of the numerical profile.

For the same rectangular arrangement, with $H_x >> H_y$, in Figs. 10 and 11, we plot the local cation distributions computed with the DFT/MSA approach along with one-dimensional profiles for x and y fixed. In a similar fashion to the electric potential, the cationic concentration tends to increase substantially in the vicinity of the particles exhibiting more pronounced sharp layers in the x-direction, where the PB approximation is accurate. On the other hand, the effects of the short-range correlations tend to reduce the boundary layers located at $y = \pm(H_y - d/2)$. A comparison between PB and DFT/MSA profiles is presented in Fig. 11. We may observe a less abrupt distribution of cations computed with DFT/MSA in the vicinity of the particles compared to the Poisson-Boltzmann profile where, owing to the point charge assumption, allows for considerable enhancement in concentration.

In order to analyze the influence of particle distance upon the profiles obtained with PB and DFT/MSA, we now consider a rectangular arrangement with larger horizontal and vertical particle distances ($H_y/d = 5$, $H_x/d = 11.75$) compared to the previous example and c_b = 0.001 M. The profiles of the correlation functions for cations obtained

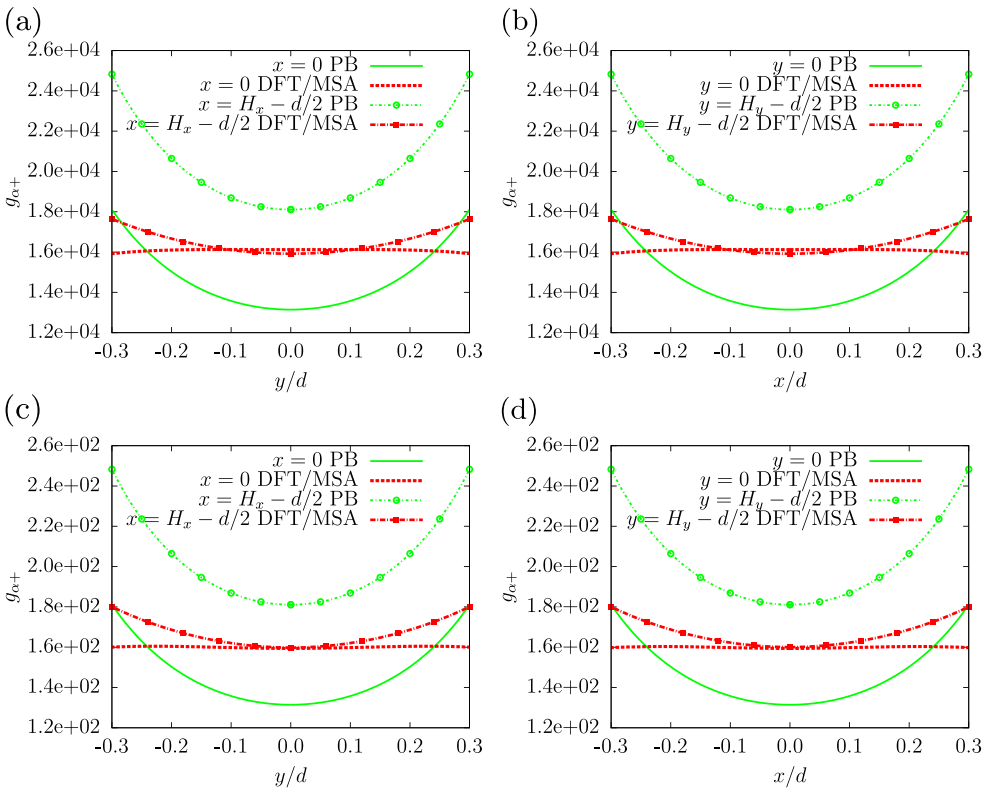

Fig. 14 Comparison between the ionic profiles computed with PB and DFT/MSA: **a**, **b** c_b = 0.001 M and **c**, **d** c_b = 0.1 M

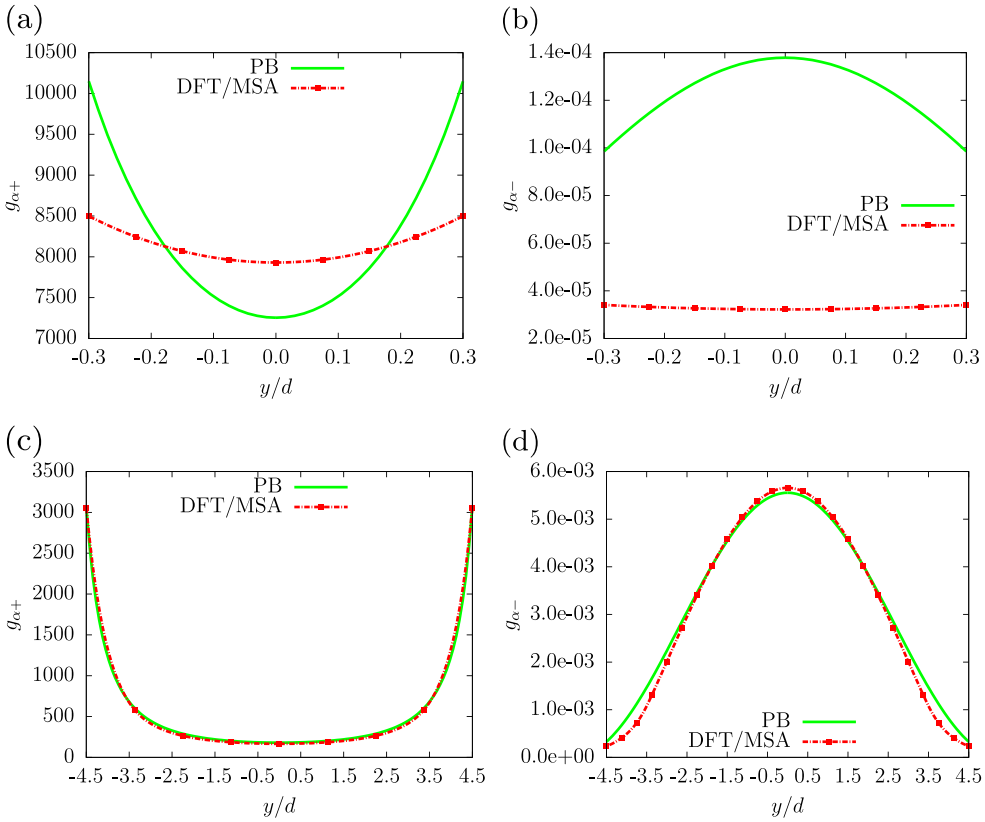

Fig. 15 Comparison between the one-dimensional monovalent ionic profiles computed with PB and DFT/MSA. Cations (**a**) and anions (**b**) for $2H_x/d = 6.4$ and $2H_y/d = 1.6$. Cations (**c**) and anions (**d**) for $2H_x/d = 23.5,\ 2H_y/d = 10$

with DFT/MSA are depicted in Fig. 12 and the 1D cuts along the coordinates planes in Fig. 13. For larger distances between particles, we may note a wider range of values of cation distribution compared to the previous case (Fig. 11a)

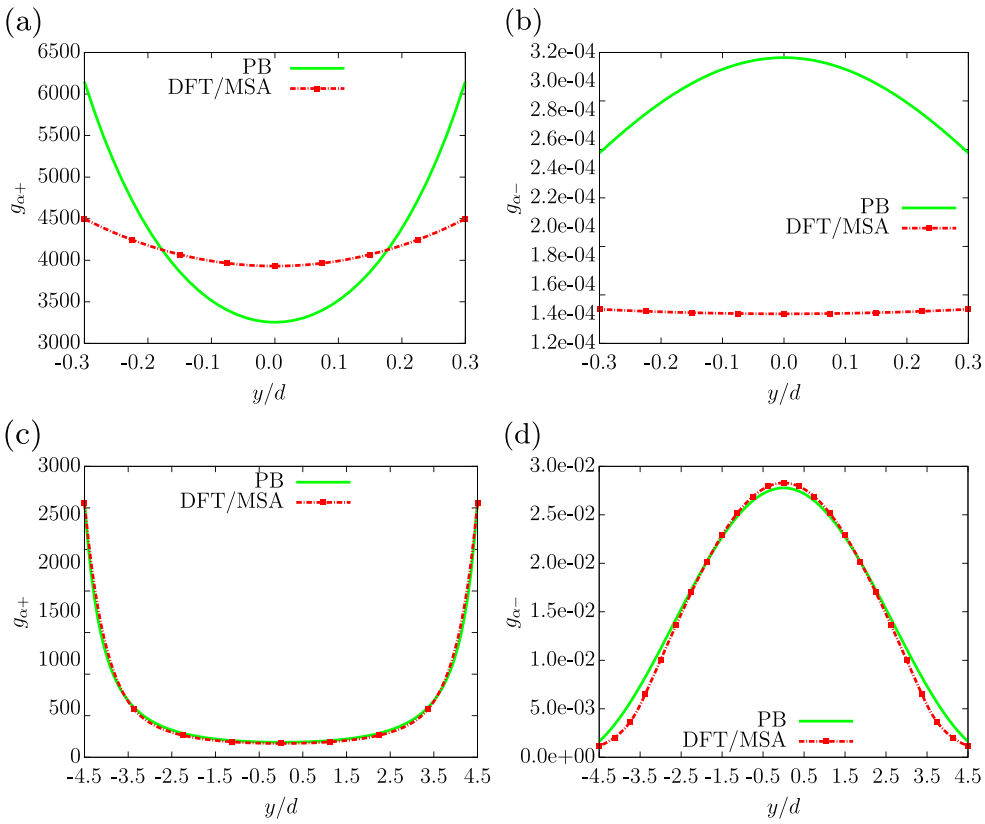

Fig. 16 Comparison between the one-dimensional bivalent ionic profiles computed with PB and DFT/MSA procedures. Cations (**a**) and anions (**b**) for $2H_x/d = 6.4,\ 2H_y/d = 1.6$. Cations (**c**) and anions (**d**) for $2H_x/d = 37,\ 2H_y/d = 10$

of nearly uniform profile. By comparing the results in the plane $x = 0$ obtained with the two models (Fig. 13), we observe that the distribution of cations and anions computed with DFT/MSA are very similar to the ones obtained by PB. In fact, for large particle distances, the influence of the short-range ion-ion direct correlation functions is somewhat less pronounced and the effects of the long range Coulombic interactions prevail.

We now illustrate the influence of the bulk fluid salinity upon the local ionic profiles. The results are displayed for the two values c_b = 0.001 M and c_b = 0.1 M in the square arrangement of small particle distances ($H_x/d = H_y/d = 0.8$). Figure 14 compares the one-dimensional ion profiles (for x and y fixed) computed with DFT/MSA and PB approaches. We may clearly observe that the DFT/MSA profiles exhibit more uniformity due to ion-ion correlations which tend to reduce the concentration near the charged walls. The treatment of point charge ions in the PB based approach leads to a substantial increase in ion density with sharper boundary layers in the vicinity of the particles. Such effect is more pronounced for lower concentration (c_b = 0.001 M) where the strength of the electrical double layer is higher.

Finally, we illustrate the ionic profiles in the limit case of long parallel particles in the x-direction separated by the distance $2H_y$. Numerically, a large value is assigned for H_x so that boundary effects have negligible influence. In Fig. 15, we show the ionic profiles for monovalent ions for small ($H_y/d = 0.8$) and large ($H_y/d = 5$) particle distances and c_b = 0.001 M. Again, we can observe discrepancies between DFT/MSA and PB: for small spacing where DFT/MSA furnishes a more uniform distribution, PB allows higher concentrations of cations near the particles (Fig. 15a). On the other hand, in a similar fashion

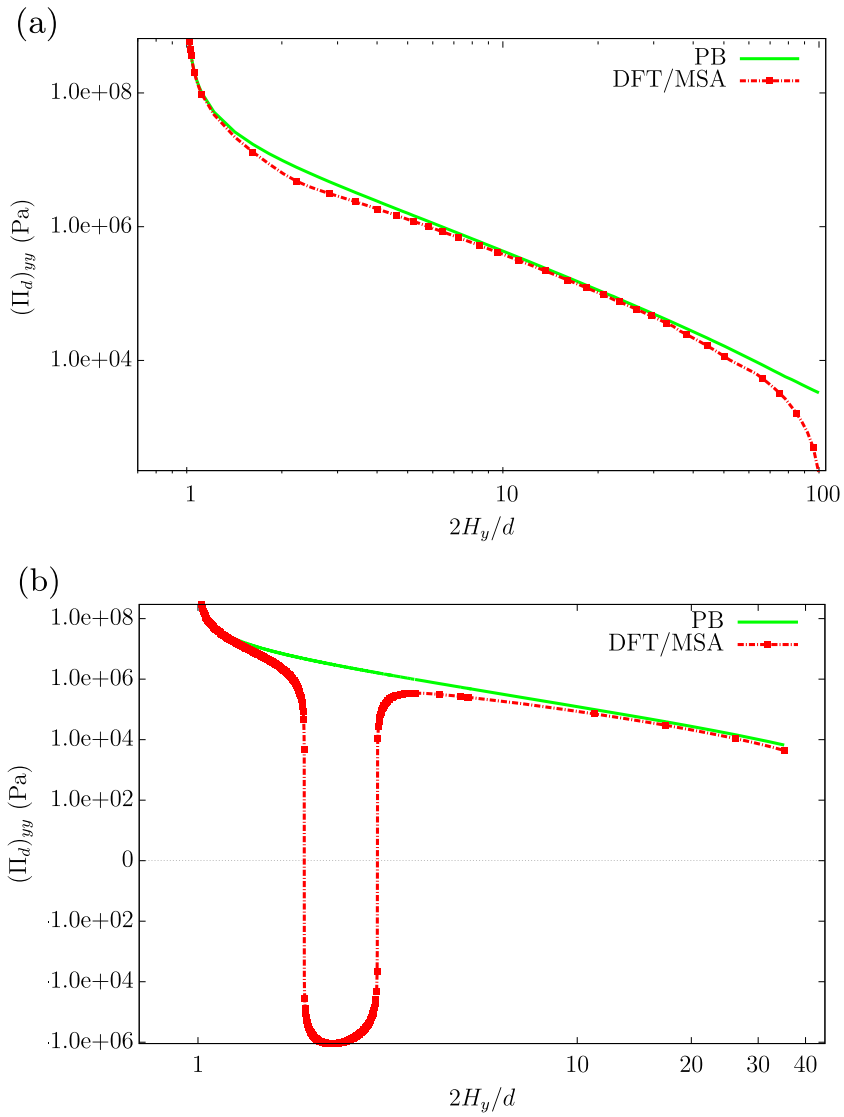

Fig. 17 Dependence of the disjoining pressure with particle separation. **a** 1:1 ions and **b** 2:2 ions

to the $2D$ case, we observe similar profiles for the two models for large particles distance (Fig. 15c, d). Finally, Fig. 16 shows the ionic profiles for divalent ions for the same small and large particle distances. We note similar behavior, however, with smaller magnitude of the correlation, as the valence $z = 2$ implies in higher value of the ion charge $q = z\,e$ which tends to reduce $g_{\alpha i}$ in order to fulfill the electroneutrality condition (13).

4.4 Disjoining pressure

We now consider the post-processing approach for computing the disjoining pressure from the contact theorem (18). The computations are carried out for the normal component $(\boldsymbol{\Pi}_d)_{yy}$ considering the stratified microstructure of infinity parallel particles. Considering now the elastic problem (21) with boundary condition (22), we approximate the mechanics by two uncoupled one-dimensional elastic problems in the x and y directions with solutions

$$(\boldsymbol{\sigma}_\pi)_{xx} = -(\boldsymbol{\Pi}_d^0)_{xx}, \quad (\boldsymbol{\sigma}_\pi)_{yy} = -(\boldsymbol{\Pi}_d^0)_{yy}\ ,$$

which from Eq. 20d imply for the swelling stress

$$(\boldsymbol{\Pi}_S)_{xx} = -\langle(\boldsymbol{\sigma}_\pi)_{xx}\rangle^s = (\boldsymbol{\Pi}_d)_{xx}\ , (\boldsymbol{\Pi}_S)_{yy} = -\langle(\boldsymbol{\sigma}_\pi)_{yy}\rangle^s = (\boldsymbol{\Pi}_d)_{yy}\ .$$

Thus, under the absence of shear stresses in the solid phase, each component of the macroscopic swelling stress tensor is nothing but the average of the respective component of the disjoining pressure.

In Fig. 17, we show the dependency of $(\boldsymbol{\Pi}_S)_{yy}$ with particle distance for the fixed salinity $c_b = 0.001$ M and compare the constitutive response for monovalent and divalent ions. For the 1:1 case, we may observe good agreement between the DFT/MSA and PB (Fig. 18) with both formulations predicting a pure repulsive stress regardless of particle distance. On the other hand, for 2:2 ions, the DFT/MSA furnishes negative values of the disjoining pressure for a particular range of particle distances giving rise to a regime dominated by attraction between the particles where the magnitude of the Maxwell component (given by the term involving the surface charge σ in Eq. 17) prevails over the kinetic one associated with the osmotic pressure. Such attraction regime, which has been reported in [37], validated experimentally and through Monte Carlo simulation (see, e.g., [4], [40]) is not captured by the PB-based model which overlooks the ionic correlation forces.

5 Conclusions

A new two-scale numerical model was proposed to compute ionic profiles and the swelling pressure in expansive porous media saturated by electrolyte solutions with mono and multivalent ions. The proposed approach was based on upscaling a non-local nanoscale model constructed within the framework of the Density Functional Theory supplemented by the mean spherical approximation. Such methodology led to a coupled Poisson-Fredholm system posed in terms of the correlation functions and electric potential. A new computational scheme was designed to discretize the nanoscale governing equations. The approximation of the nonlinear Gauss-Poisson problem was conducted in a staggered fashion by delaying the component of the source term involving the correlations. For the computation of these latter unknowns, we made use of the expansion in terms of the eigenpairs of the kernels. Such eigenfunctions were chosen as basis function for the collocation scheme adopted in the discretization of the Fredholm equation. The nonlinearities in the discrete Gauss-Poisson and integral problems were handled by the Newton and Picard schemes respectively. Computational simulations of the ionic profiles in two-dimensional geometries and the numerical reconstruction of the constitutive law of the swelling pressure, which appears in a modified form of Terzaghi effective principle, were presented showing improvement obtained with DFT/MSA compared to the Poisson-Boltzmann based approach. The computational model proposed herein provides new directions for bridging the local effects of ionic correlation in multivalent ionic solutions and the stress partitioning mechanisms in swelling clay soils ruled by the modified form of the effective stress principle.

Acknowledgments This work was supported, in part, by the CAPES-COFECUB (Project 746-12) and Fundação Araucária (Project 39.591).

Appendix A: Representation of the Kernels in rectangular arrangements

For a precise representation of the kernels $\overline{K}$ and $\widehat{K}$, we consider the rectangular arrangement depicted in Fig. 18. The plates are separated by distance $2H_x$ and $2H_y$ in the horizontal and vertical directions, respectively. The ionic species 1 and 3, located at $\boldsymbol{r} = (x, y)$ and $\boldsymbol{r} = (x', y')$, respectively, are represented by ions 1 and 3 in Fig. 18, whereas the subscript 2 represent the plates.

The closure relation for the ion-particle correlation function reads as

$$g_{\alpha i}(\boldsymbol{r}) = \exp\left\{-\beta\, q_i\, \psi(\boldsymbol{r}) + \sum_m \rho_m^b \int \widetilde{c}_{im}(|\boldsymbol{r} - \boldsymbol{r}'|)\, h_{\alpha m}(\boldsymbol{r}')d\boldsymbol{r}'\right\}, \tag{A.1}$$

where

$$\widetilde{c}_{im}(\boldsymbol{r}) = c_{hs}(|\boldsymbol{r}|) + \frac{\beta e^2 z_i z_m}{4\pi\widetilde{\varepsilon}\widetilde{\varepsilon}_0 d}\, c_d^{sr}(|\boldsymbol{r}|)\ . \tag{A.2}$$

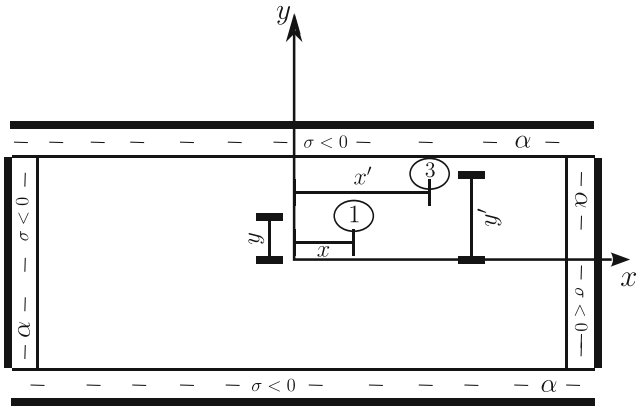

Fig. 18 Rectangular unit cell geometry for computation of the kernels

As the direct correlation functions $c_{hs}(\boldsymbol{r})$ and $c_d^{sr}(\boldsymbol{r})$ have support $|\boldsymbol{r}| \leq d$, the integration is limited to the interior of the rectangle ($|x| < H_x$ and $|y| < H_y$). By exploring the symmetry $h_{\alpha m}(x, y) = h_{\alpha m}(-x, y) = h_{\alpha m}(x, -y)$, the above representation can be rewritten in the form:

$$\begin{aligned} g_{\alpha i}(x, y) = \exp\Bigg\{ & -\beta\, q_i\, \psi(x, y) + \int_0^{H_y - \frac{d}{2}} \int_0^{H_x - \frac{d}{2}} \\ & \times K_{+i}(x, y, x', y')\, h_{\alpha +}(x', y')\, dy'\, dx' \\ & + \int_0^{H_y - \frac{d}{2}} \int_0^{H_x - \frac{d}{2}} K_{-i}(x, y, x', y') \\ & \times h_{\alpha -}(x', y')\, dy'\, dx' + J(x, y) \Bigg\}, \; i = \{+, -\} \end{aligned} \tag{A.3}$$

where the term $J(x, y)$ is defined by

$$\begin{aligned} J(x, y) = & -\int_{H_y - \frac{d}{2}}^{H_y + \frac{d}{2}} \int_0^{H_x + \frac{d}{2}} M(x, y, x', y') \sum_m \rho_m^b\, dy'\, dx' \\ & -\int_0^{H_y - \frac{d}{2}} \int_{H_x - \frac{d}{2}}^{H_x + \frac{d}{2}} M(x, y, x', y') \sum_m \rho_m^b\, dy'\, dx' \end{aligned} \tag{A.4}$$

and each kernel given by

$$K_{\pm i}(x, y, x', y') = \rho_{\pm}^b \left[M(x, y, x', y') + z_i\, z_{\pm}\, L(x, y, x', y') \right]. \tag{A.5}$$

Thus, we are led to compute the two functions M and L which incorporate the hard-sphere and electrostatic component of the short-range direct correlation $\widetilde{c}_{im}$ in Eq. B.5. The component M is defined by

$$M(x, y, x', y') = \sum_{j=1}^{4} M^j(x, y, x', y')$$

where each component $j \in \{1, 2, 3, 4\}$ is given by

$$\begin{aligned} M^j(x, y, x', y') &= \int_{-\infty}^{\infty} c_{hs}\left(\sqrt{r_j^2 + z'^2}\right) dz' \\ &= \begin{cases} \displaystyle\int_{-\sqrt{d^2 - r_j^2}}^{\sqrt{d^2 - r_j^2}} c_{hs}\left(\sqrt{r_j^2 + z'^2}\right) dz' & \text{if } r_j^2 < d^2\,, \\ 0 & \text{if } r_j^2 > d^2\,, \end{cases} \end{aligned} \tag{A.6}$$

with

$$r_1^2 = (x - x')^2 + (y - y')^2\,, \tag{A.7a}$$
$$r_2^2 = (x - x')^2 + (y + y')^2\,, \tag{A.7b}$$
$$r_3^2 = (x + x')^2 + (y - y')^2\,, \tag{A.7c}$$
$$r_4^2 = (x + x')^2 + (y + y')^2\,. \tag{A.7d}$$

In a similar fashion, L is given by replacing c_{hs} by $\beta e^2/(4\pi\widetilde{\varepsilon}\widetilde{\varepsilon}_0 d) c_d^{sr}$ in Eq. A.6.

Recalling the representation (B.6) for the hard-sphere component $c_{hs}(r)$, it follows that

$$\begin{aligned} M^j(x, y, x', y') &= \int_{-\sqrt{d^2 - r_j^2}}^{\sqrt{d^2 - r_j^2}} \left[a_1 + a_2 \left(\frac{r_j}{d} \sqrt{1 + \left(\frac{z'}{r_j}\right)^2} \right) \right. \\ &\qquad \left. + a_3 \left(\frac{r_j}{d} \sqrt{1 + \left(\frac{z'}{r_j}\right)^2} \right)^3 \right] dz' \\ &= m_{j1} + m_{j2} + m_{j3}\,. \end{aligned} \tag{A.8}$$

By performing the integrations, each component admits the representation

$$m_{j1} = 2\, a_1\, d \sqrt{1 - r_j^{*2}}\,,$$

$$m_{j2} = a_2\, d \left[\sqrt{1 - r_j^{*2}} + r_j^{*2} \log\left(\frac{1 + \sqrt{1 - r_j^{*2}}}{r_j^*} \right) \right],$$

$$m_{j3} = \frac{a_3\, d}{2} \left[\left(1 + \frac{3}{2} r_j^{*2} \right) \sqrt{1 - r_j^{*2}} + \frac{3}{2} r_j^{*4} \log\left(\frac{1 + \sqrt{1 - r_j^{*2}}}{r_j^*} \right) \right],$$

with $r_j^{*2} = r_j^2/d^2$. Adopting the same procedure replacing c_{hs} by $\beta e^2/(4\pi\widetilde{\varepsilon}\widetilde{\varepsilon}_0 d) c_d^{sr}$, we have for the electrostatic component of the kernel

$$\begin{aligned} L^j(x, y, x', y') &= \frac{\beta\, e^2}{4\pi\widetilde{\varepsilon}\widetilde{\varepsilon}_0 d} \int_{-\sqrt{d^2 - r_j^2}}^{\sqrt{d^2 - r_j^2}} c_d^{sr} \left(r_j \sqrt{1 + \left(\frac{z'}{r_j}\right)^2} \right) dz', \\ j &= 1, 2, 3, 4\,. \end{aligned}$$

By inserting the representation (B.7) for $c_d^{sr}(r)$ and performing the integrals, we arrive at

$$L^j(x,y,x',y') = \frac{\beta e^2}{4\pi\widetilde{\varepsilon}\widetilde{\varepsilon}_0 d}\int_{-\sqrt{d^2-r_j^2}}^{\sqrt{d^2-r_j^2}} \times\left[\frac{d}{\sqrt{r_j^2+z'^2}}-2B+\frac{B^2}{d}\sqrt{r_j^2+z'^2}\right]dz' = \frac{\beta e^2}{4\pi\widetilde{\varepsilon}\widetilde{\varepsilon}_0 d}\left(l_{j1}+l_{j2}+l_{j3}\right) ,$$

with l_{j1}, l_{j2} and l_{i3} given by

$$l_{j1} = 2d\log\left(\frac{1+\sqrt{1-r_j^{*2}}}{r_j^*}\right) ,$$

$$l_{j2} = -4Bd\sqrt{1-r_j^{*2}} ,$$

$$l_{j3} = B^2 d\left[\sqrt{1-r_j^{*2}}+r_j^{*2}\log\left(\frac{1+\sqrt{1-r_j^{*2}}}{r_j^*}\right)\right] .$$

Finally, inserting the representations for M and L in Eq. A.5, we obtain for the kernel

$$K_{\pm i}(x,y,x',y') = \rho_\pm^b\sum_{j=1}^{4}\begin{cases} 2a_1 d\sqrt{1-r_j^{*2}}+ \\ a_2 d\left[\sqrt{1-r_j^{*2}}+\frac{r_j^{*2}}{2}\log\left(\frac{1+\sqrt{1-r_j^{*2}}}{1-\sqrt{1-r_j^{*2}}}\right)\right] \\ \frac{a_3 d}{2}\left[\left(1+\frac{3}{2}r_j^{*2}\right)\sqrt{1-r_j^{*2}}+\frac{3}{4}r_j^{*4}\log\left(\frac{1+\sqrt{1-r_j^{*2}}}{1-\sqrt{1-r_j^{*2}}}\right)\right] \\ +\frac{\beta z_i z_\pm e^2}{4\pi\widetilde{\varepsilon}\widetilde{\varepsilon}_0 d}\left[d\log\left(\frac{1+\sqrt{1-r_j^{*2}}}{1-\sqrt{1-r_j^{*2}}}\right)-4Bd\sqrt{1-r_j^{*2}}\right. \\ \left.+B^2 d\left[\sqrt{1-r_j^{*2}}+\frac{r_j^{*2}}{2}\log\left(\frac{1+\sqrt{1-r_j^{*2}}}{1-\sqrt{1-r_j^{*2}}}\right)\right]\right], \quad \text{if } r_j^*<1 , \\ 0, \quad \text{if } r_j^*>1 . \end{cases} \tag{A.9}$$

Note that, due to the square dependence of r_j^2 on coordinates (x,y,x',y') in Eq. (A.7), the kernels are symmetric,

$$K_{\pm i}(x,y,x',y') = K_{\pm i}(x',y',x,y) . \tag{A.10}$$

Appendix B: Representations of the free energy and direct correlation function

Our aim in this section is to derive the expression for the free energy functional in terms of the correlation function $c_{im}^{(2)}(\boldsymbol{r},\boldsymbol{r}')$. To this end, we begin by integrating (2) using a linear path for the density variation parametrized by the Onsager parameter ξ $(0\le\xi\le)$,

$$\rho_i(\boldsymbol{r},\xi) = \rho_i^b + \xi\Delta\rho_i(\boldsymbol{r})$$

where $\Delta\rho_i(\boldsymbol{r}) = \rho_i(\boldsymbol{r}) - \rho_i^b$. This yields

$$\mathcal{F}^{ex}[\rho_i] = (\mathcal{F}^b)^{ex} - k_B T\int_0^1 d\xi\sum_i\int\Delta\rho_i(\boldsymbol{r})c_i^{(1)}(\boldsymbol{r},\xi)d\boldsymbol{r} . \tag{B.1}$$

In an analogous manner, by integrating (2), it follows that

$$c_i^{(1)}(\boldsymbol{r},\xi) = c_i^{(1)}|^b(\boldsymbol{r}) + \sum_m\int_0^{\xi'}d\xi'\int\Delta\rho_m(\boldsymbol{r}')c_{im}^{(2)}(\boldsymbol{r},\boldsymbol{r}',\xi)d\boldsymbol{r}' . \tag{B.2}$$

Thus, using (B.2) in Eq. B.1, we obtain

$$\mathcal{F}^{ex}[\rho_i] = (\mathcal{F}^b)^{ex} - k_B T\int_0^1 d\xi\sum_i\int\Delta\rho_i(\boldsymbol{r})c_i^{(1)}|^b(\boldsymbol{r})d\boldsymbol{r} - k_B T\int_0^1 d\xi\sum_{i,m}\int_0^{\xi'}d\xi'\int\int\Delta\rho_i(\boldsymbol{r})\Delta\rho_m \times(\boldsymbol{r}')c_{im}^{(2)}(\boldsymbol{r},\boldsymbol{r}',\xi)d\boldsymbol{r}d\boldsymbol{r}' . \tag{B.3}$$

Now, recalling the thermodynamic definition of the chemical potential, we obtain for the excess component of this quantity

$$(\mu_i)^{ex} = \frac{\delta\mathcal{F}^{ex}[\rho_i]}{\delta[\rho_i(\boldsymbol{r})]} = -k_B T c_i^{(1)}(\boldsymbol{r}) .$$

Using the above relation in (B.3) gives

$$\mathcal{F}^{ex}[\rho_i] = (\mathcal{F}^b)^{ex} + \sum_i(\mu_i^b)^{ex}\int\Delta\rho_i(\boldsymbol{r})d\boldsymbol{r} - k_B T\int_0^1 d\xi\sum_{i,m}\int_0^{\xi'}d\xi'\int\int\Delta\rho_i(\boldsymbol{r})\Delta\rho_m \times(\boldsymbol{r}')c_{im}^{(2)}(\boldsymbol{r},\boldsymbol{r}',\xi)d\boldsymbol{r}d\boldsymbol{r}' .$$

From integration by parts, we have for any function $y(\xi)$:

$$\int_0^1 d\xi\int_0^\xi y(\xi')d\xi' = \int_0^1(1-\xi)y(\xi)d\xi .$$

Therefore, we obtain

$$\mathcal{F}^{ex}[\rho_i] = (\mathcal{F}^b)^{ex} + \sum_i (\mu_i^b)^{ex} \int \Delta\rho_i(\boldsymbol{r}) d\boldsymbol{r} - k_B T \sum_{i,m} \int_0^1 d\xi (1-\xi) \int\int \Delta\rho_i(\boldsymbol{r}) \Delta\rho_m \times (\boldsymbol{r}') c_{im}^{(2)}(\boldsymbol{r}, \boldsymbol{r}', \xi) d\boldsymbol{r} d\boldsymbol{r}' \ .$$

The closure issue for $c_{im}^{(2)}(\boldsymbol{r}, \boldsymbol{r}', \xi)$ is seated on the Mean Spherical Approximation (MSA) in the bulk fluid [45, 46] and postulates independence of $c_{im}^{(2)}(\boldsymbol{r}, \boldsymbol{r}', \xi)$ on the Onsager parameter ($c_{im}^{(2)}(\boldsymbol{r}, \boldsymbol{r}', \xi) \approx c_{im}^b(|\boldsymbol{r} - \boldsymbol{r}'|)$). Under this assumption, we obtain

$$\mathcal{F}^{ex}[\rho_i] = (\mathcal{F}^b)^{ex} + \sum_i (\mu_i^b)^{ex} \int \Delta\rho_i(\boldsymbol{r}) d\boldsymbol{r} - k_B T \sum_{i,m} \int_0^1 d\xi (1-\xi) \int\int \Delta\rho_i(\boldsymbol{r}) \Delta\rho_m \times (\boldsymbol{r}') c_{im}^b(\boldsymbol{r}, \boldsymbol{r}') d\boldsymbol{r} d\boldsymbol{r}'.$$

Moreover, in the context of the MSA closure, $c_{im}^b(\boldsymbol{r}) = c_{im}^{MSA}(r)$ is written as the sum of a Coulombic term and an additional short-range component $\widetilde{c}_{im}(r)$ which vanishes for $r > d$

$$c_{im}^{\mathrm{MSA}}(r) = \begin{cases} \widetilde{c}_{im}(r) - \dfrac{\beta z_i \, z_m \, e^2}{4\pi \, \widetilde{\varepsilon}\widetilde{\varepsilon}_0 \, r} & \text{for } r < d \\ - \dfrac{\beta z_i \, z_m \, e^2}{4\pi \, \widetilde{\varepsilon}\widetilde{\varepsilon}_0 \, r} & \text{for } r > d \ , \end{cases} \tag{B.4}$$

The short-range component $\widetilde{c}_{im}(r)$ is given by the sum of the classical hard spheres component $c_{hs}(r)$ [47] and of a short-range electrostatic correction $c_d^{sr}(r)$ (relative to the Coulomb term due to the finite size of the ions). We then have [45, 46].

$$\widetilde{c}_{im}(r) = \begin{cases} c_{hs}(r) + \dfrac{\beta \, z_i \, z_m \, e^2}{4\pi \, \widetilde{\varepsilon}\widetilde{\varepsilon}_0} \, c_d^{sr}(r) & \text{for } r < d \\ 0 & \text{for } r > d \ . \end{cases} \tag{B.5}$$

The hard sphere component is given by (see [43, 47] for details)

$$c_{hs}(r) = \begin{cases} a_1 + a_2 \dfrac{r}{d} + a_3 \dfrac{r^3}{d^3} & \text{for } r < d, \\ 0 & \text{for } r > d \ , \end{cases} \tag{B.6}$$

where $\eta = (\rho\pi \, d^3)/6$ is the packing fraction, given by the volume fraction occupied by the hard spheres, and

$$a_1 = -\frac{(1+2\eta)^2}{(1-\eta)^4}, \quad a_2 = 6\eta \frac{(1+0.5\eta)^2}{(1-\eta)^4}, \quad a_3 = \frac{\eta}{2} a_1 \ .$$

The function $c_d^{sr}(r)$ incorporates the short range correction of the Coulomb term (see [45, 46])

$$c_d^{sr}(r) = \begin{cases} \dfrac{d}{r} - 2\,B + B^2 \dfrac{r}{d} & \text{for } r < d \\ 0 & \text{for } r > d \ , \end{cases} \tag{B.7}$$

with the inverse of the Debye length κ and B given by

$$\kappa^2 = \frac{\beta}{\widetilde{\varepsilon}\widetilde{\varepsilon}_0} \sum_m \rho_m^b \, (z_m \, e)^2 \ ,$$

$$B = \frac{x^2 + x - x\sqrt{1+2x}}{x^2} \quad \text{with} \quad x = \kappa \, d \ .$$

References

1. Attard, P.: Thermodynamics and Statistical Mechanics: Equilibrium by Entropy Maximisation. Academic Press, London (2002)
2. Biot, M.A.: General Theory of Three-dimensional Consolidation. J. Appl. Phys. **12**(2), 155–164 (1941)
3. Carnie, S., Chan, Y.: The statistical mechanics of the electrical double layer: stress tensor and contact conditions. J. Chem. Phys. **74**(2), 1293–1297 (1981)
4. Ebeling, D., van den Ende, D., Mugele, F.: Electrostatic interaction forces in aqueous salt solutions of variable concentration and valency. Nanotechnology **22**(30), 305706 (2011)
5. Derjaguin, B.V., Churaev, N., Muller, V.: Surface Forces. Plenum Press, New York (1987)
6. Dormieux, L., Lemarchand, E., Coussy, O.: Macroscopic and micromechanical approaches to the modelling of the osmotic swelling in clays. Transp. Porous Media **50**, 75–91 (2003)
7. Evans, R.: The nature of the Liquid-Vapor interface and other topics in the statistical mechanics of Non-Uniform, kclassical fluids. Adv. Phys. **28**(2), 143–200 (1979)
8. Hackbusch, W.: Integral Equations. Theory and Numerical Treatment, Birkhäuser, Basel (1995)
9. Hansen, J.-P., McDonald, I.R.: Theory of Simple Liquids, Third Edition, Elsevier (2006)
10. Hill, T.L.: Statistical Mechanics: Principles and Selected Applications. McGraw-Hill Book Company, Inc, New York 1956 Reprinted by Dover Publications (1987)
11. Irving, J.H., Kirkwood, J.: The statistical mechanical theory of transport processes. IV. The equation of hydrodynamics. J. Chem. Phys. **18**(6), 817–829 (1950)
12. Kjellander, R., Marčelja, S., Pashley, R.M., Quirk, J.P.: Double layer ion correlation forces restrict calcium-clay swelling. J. Phys. Chem. **92**, 6489–6492 (1988)
13. Kjellander, R., Pashley, R.M., Quirk, J.P., Theoretical, A.: Experimental study of forces between charged Mica surfaces in aqueous $CaCl_2$ solutions. J. Chem Phys. **92**(7), 4399–4407 (1990)
14. Lai, W.M., Hou, J.S., Mow, V.C.: A triphasic theory for the swelling and deformation behaviors of articular cartilage. ASME J. Biomech. Eng. **113**, 245–258 (1991)
15. Le, T.D., Moyne, C., Murad, M.A., Lima, S.A.: A two-scale non-local model of swelling porous media incorporating ion size correlation effects. J. Mech. Phys. Solids **61**(12), 2493–2521 (2013)
16. Le, T.D., Moyne, C., Murad, M.A.: A three-scale model for ionic solute transport in swelling clays incorporating ion-ion correlation effects. Adv. Water Resour. **75**, 31–52 (2015)
17. Lyklema, J.: Fundamentals of Colloid and Interface Science. Academic, London (1993)

18. Looker, J.R., Carnie, S.L.: Homogenization of the ionic transport equations in periodic porous media. Transp. Porous Media **65**, 107–131 (2006)
19. Lozada-Cassou, M.: The force between two planar electrical double layers. J. Chem. Phys. **80**(7), 3344–3349 (1984)
20. Lozada-Cassou, M., Díaz-herrera, E.: Three point extension for the hypernetted chain and other integral equation theories. J. Chem. Phys. **92**(2), 1194–1210 (1990)
21. McQuarrie, D.A.: Statistical Mechanics, University Science Books (2000)
22. Mier-y-Teran, L., Suh, S.H., White, S., Davis, H.T.: A non-local free-energy density-functional approximation for the electrical double layer. J. Chem. Phys. **92**(8), 5087–5098 (1990)
23. Mitchell, J.K.: Fundamentals of Soil Behaviour, John Wiley & Sons Inc. (1993)
24. Mody, F.K., Hale, A.H.: A borehole stability model to couple the mechanics and chemistry of drilling fluid shale interaction, Paper SPE/IADC 25728 Society of Petroleum Enginneers, 473–489 (1993)
25. Moyne, C., Murad, M.A.: Electro-chemo-mechanical couplings in swelling clays derived from Micro/Macro homogenization procedure. Int. J. Solids Struct. **39**, 6159–6190 (2002)
26. Moyne, C., Murad, M.A.: Macroscopic behaviour of swelling porous media derived from micromechanical analysis. Transp. Porous Media **50**, 127–151 (2003)
27. Moyne, C., Murad, M.A.: A two-scale model for coupled electro-chemo-mechanical phenomena and onsager's reciprocity relations in expansive clays: i homogenization analysis. Transp. Porous Media **62**, 333–380 (2006)
28. Moyne, C., Murad, M.A.: A two-scale model for coupled electro-chemo-mechanical phenomena and onsager's reciprocity relations in expansive clays: II computational validation. Transp. Porous Media **63**, 13–56 (2006)
29. Murad, M.A., Moyne, C.: Micromechanical computational modeling of expansive porous media. C. R. Mecanique **330**, 865–870 (2002)
30. Murad, M.A., Moyne, C.: A dual-porosity model for ionic solute transport in expansive clays. Comput. Geosci. **12**, 47–82 (2008)
31. Nelson, J.D., Miller, D.J.: Expansive soils: Problem and Practice in Foundation and Pavement Engineering, John Wiley & Sons Inc. (1992)
32. Nickell, R.E., Gartling, D.K., Strang, G.: Spectral decomposition in advection-diffusion analysis by finite element methods. Comput. Methods Appl. Mech. Eng. **17-18**, 561–580 (1979)
33. Oliveira, S.P., Azevedo, J.S.: Spectral element approximation of Fredholm integral eigenvalue problems. J. Comput. Appl. Math. **257**, 46–56 (2014)
34. Ort, V.: On the physical and chemical stability of shales. J. Pet. Sci. Eng. **38**(3–4), 213–235 (2003)
35. Ponce, R.V., Murad, M.A., Lima, S.: A two-scale computational model of pH sensitive expansive porous media. J. Appl. Mech. **80**(2), 0209031–2090314 (2013)
36. Quesada-Pérez, M., González-Tovar, E., Martín-molina, A., Lozada-Cassou, M., Hidalgo-Álvarez, R.: Overcharging in colloids: beyond the Poisson-Boltzmann approach. ChemPhysChem **4**(3), 234–248 (2003)
37. Jellander, R., Marčelja, S., Quirk, J.P.: Attractive double-layer interactions between calcium clay particles. J. Colloid Interface Sci. **126**(01), 194–211 (1988)
38. Rowe, R.K.: Long-term performance of contaminant barrier systems. Geotechinique **35**(09), 631–678 (2005)
39. Ruhl, J.L., Daniel, D.E.: Geosynthetic clay liners permeated with chemical solutions and leachates. J. Geotech. Geoenviron. Eng. **123**, 369–381 (1997)
40. Segad, M., Jönsson, B., Åkesson, T., Cabane, B.: Ca/Na montmorillonite: structure, forces and swelling properties. Langmuir **26**(08), 5782–5790 (2010)
41. Zixiang, T., Mier-y-Teran, L., Davis, H.T., Scriven, L.E., White, H.S.: Non-local free-energy density-functional theory applied to the electrical double layer. Part I: Symmetrical electrolytes. Mol. Phys. **71**(2), 369–392 (1990)
42. Zixiang, T., Scriven, L.E., Davis, H.T.: Interactions between primitive electrical double layers. J. Chem. Phys. **97**(12), 9258–9266 (1992)
43. Thiele, E.: Equation of state of hard spheres. J. Chem. Phys. **39**(2), 474–479 (1963)
44. Van Olphen, H.: An Introduction to Clay Colloid Chemistry: For Clay Technologists, Geologists, and Soil Scientists. Wiley, New York (1977)
45. Waisman, E., Lebowitz, J.L.: Mean spherical model integral equation for charged hard spheres. I. Method of solution. J. Chem. Phys. **56**(6), 3086–3093 (1972)
46. Waisman, E., Lebowitz, J.L.: Mean spherical model integral equation for charged hard spheres. II. Results. J. Chem. Phys. **56**(6), 3093–3099 (1972)
47. Wertheim, M.S.: Exact solution of the Percus-Yevick integral equation for hard spheres. Phys. Rev. Lett. **10**(8), 321–323 (1963)